Technical article

The art of modelling Electrical Machines

***Abstract* — Up to date, numerical techniques for "low frequency" electromagnetic questions have been employed extensively for all possible types of application. Due to its complicated geometry on the one hand, the numerical computation of electrical machines was always and is still challenging. On the other hand, maximum conditions e.g. the aspect ratio of the device's dimensions can be numerically troublesome and can let 3d numerical models grow up to huge systems which are difficult to handle. Furthermore, the modelling of particular physical effects can be difficult due to the particular boundary conditions in time or space, which must be fulfilled.**

In the beginning of Computational Electromagnetics, many authors amongst others the well known Peter Silvester [52] introduced to the engineering community the Finite Element Method (FEM) in mathematical theory and by useful Fortran program code. On this basis, the fundamental questions of stationary, harmonic or transient behaviour of electromagnetic devices could be tackled at that time. The FEM was ready for electric motor simulations [43]. Refinements and extensions of the FEM followed up to day. With increasing computational power, model refinements to the class of coupled problems appeared [29]. This coupling of physical effects by numerical models allows to better understand the device's behaviour. Methods are coupled to methods to e.g. increase the computational velocity of the solution process. An attempt for a systematic classification of coupled problems can be found in [28]. However, the main goal of such efforts was to explore an overall behaviour of the device under study including all possible physical side effects simultaneously. As a consequence of this coupling approach, confusing many parameters describe the device under study. To unscramble the impact of the parameters, numerical models are developed to answer very specific questions [47].

From the numerical magnetic field solution derived parameters, such as e.g. inductivities, representing another class of model, help to understand the interrelation between physical effect, its mode of operation and its particular source. Therefore, such analytical approaches as the lumped parameter model, are still valuable for the understanding. Numerical solutions deliver the accurate overall result of a field problem, reflecting the state of energy in the electromagnetic device. However, the inference from that numerical solution back to the single source of effects is not possible. The coupled approach, having simultaneously all sources considered in a large numerical model does not allow to fully understand the detailed behaviour of the device and its dependency on the outer parameters. To cope with this dependency of parameters carefully to the final results, subproblems have to be defined, which employ particular boundary conditions to consider or not single sources respectively physical effects. As a consequence, a lot of simulations with meaningful parameter variations have to be performed to fully understand the device under study in the physical way. By spending such efforts, it is possible to determine important parameters which dominate the behaviour of the electromagnetic device. Things are getting more complicated by considering coupling effects which are of thermal or mechanical origin.

Another way to cope with the mentioned problem of identifying and evaluating parameters is to develop a methodology to couple the numerical approach to analytical models. With this approach it is possible to separate a physical source from its effect in the model. This provides the possibility of determining the significant model parameter and its mutual interaction with others. Due to particular limitations of analytical models, for example such as non-linearity or complicated geometry, this approach is not in general applicable. However, particular and specific problems can be solved in an efficient way. This paper is a contribution which represents a methodology to better understand an electromagnetic device, such as an electric motor, and which enables to give an innovative impulse to the aspects of computation in electromagnetics.

I Introduction

The modelling of electrical machines is described and presented in a large pool of scientific publications and its area of science offers a large treasure trove of experience. Both, analytical models as well as numerical models are used to compute the behaviour of the motor devices.

The main goal of a numerical field simulation is to explore the overall behaviour of the device under study, including all possible physical side effects simultaneously.

Numerical field solutions deliver the accurate overall result of a field problem, reflecting the state of energy in the electromagnetic device. However, the inference from the final numerical solution back to the single source of effects is not possible. To understand the behaviour of the electric motor and to be able to enhance it, the accurate knowledge of the parameters governing the physical effect must be known. So called coupled problems can distinguish between the single effects and may help to better understand the effects and their mode of operation. The coupling of methods plays an important role [28]. As a consequence of a coupled approach, confusing many parameters describe now the device under study. To unscramble the impact of the parameter, specific models are developed to answer the very specific questions. Such particular models are discussed in this contribution.

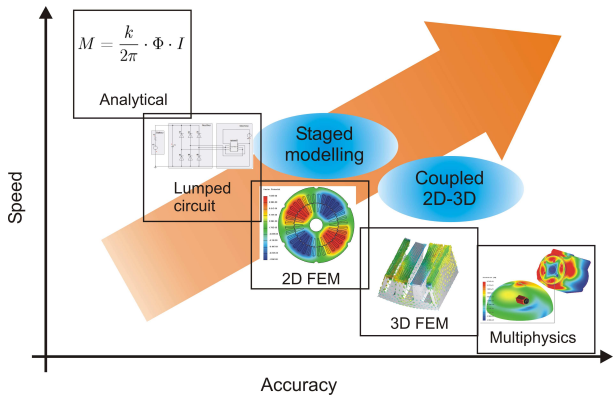

Figure 1: Speed vs. accuracy of various field computation approaches.

Figure 1 shows the computational speed versus the obtained accuracy of various field computational approaches. Analytical models are of course fast when compared to the multi physics approach. The coupling of the field simulation methods is a possible way to obtain fast and accurate field computation.

In this contribution we want to present exemplarily, in which way electrical machines can be modelled in an efficient way and want to reveal that analytical models are still valuable to advocate the physical understanding of the device under study. On the other hand, the coupling of analytical and numerical models can reduce the overall computational efforts significantly. Lumped parameter models e.g. arranged in an iterative loop with a numerical FE model shorten the computation time and at the same time enable the possibility of having a very fast parameter model of the machine to determine its dynamic behaviour.

This article is therefore organised as follows. The typical design process of an electrical machine, in our case based on an automated FE-calculation chain, is presented in section II. The existence of a valid design candidate is assumed. The result –

possibly after a set of design iterations – is a machine geometry and operating figures as e.g. power losses or efficiency. This data can subsequently be used in the analysis of advanced design aspects as for instance a cause-effect dependency analysis, presented in section III. The conjunction between cause and effect there is built using an extended conformal mapping approach. Equally important to a cause-effect dependency analysis is a detailed investigation of the iron losses inside the machine, separating the overall iron losses into eddy current losses and hysteresis losses. A possible approach for this purpose is given in section IV. The therein first stated course of action however still is based on analytical post-processing formulae, neglecting the hysteretic material behaviour in the field model and assuming a homogeneous magnetic field distribution across the lamination. An improved approach can be based on a coupled magneto-dynamic vector hysteresis model, as explained in the section's end. Such a model nevertheless requires a solver providing the magnetic scalar potential in 3D for rotating machines. As a consequence, section V presents some ideas for a possible generic solver approach. Until here, all calculations and considerations have been based on the assumption of ideal machines, which present geometrical and electric symmetric properties. The considered air-gap field of the device under study hence shows a spatial periodicity along its circumference and iterates in dependence of a certain angle. Reality however shows that – due to tolerances in the manufacturing process and other deviations – the assumption of an iterating air-gap field is not valid. Section VI accordingly deals with possibilities to include such stochastic considerations into the presented design chain. A typical consequence of these stochastic deviations is the rise of new harmonic orders, resulting in torque ripple, losses and noise in particular. On these grounds section VII gives some insight in the calculation of machine acoustics. Upon this, section VIII shows in which way the produced results can be displayed in a virtual reality environment and how to manipulate them interactively. Section IX concludes with the determination of lumped parameters, as they are required for building dynamic control models of the machine in their later use and leads to a final summary.

II Design process

During the design process of an electrical machine different calculation tools must be combined according to the specific machine requirements, the design goals and the requirements of the application. Each set of these three design aspects demands for a certain combination of the respective tools.

Figure 2 shows the design approach for calculating a two-dimensional efficiency map of a permanent magnet synchronous motor (PMSM). After the efficiency map is calculated, further design aspects can be analysed (sections VI - VII) and the results can be presented by means of virtual reality (section VIII).

To minimise the time required for the design process an automated design approach and parallel computing is introduced. As an example, the automated design process for calculating the efficiency map is presented. Simulations include losses and the evaluation of inductances which are discussed in sections IV and IX in detail.

A Automatisation

Figure 2 contains a flowchart describing an automated process for the calculation of all relevant machine characteristics to generate a two-dimensional efficiency map. In the following, the function of each block from this graph is briefly described. A detailed explanation is presented in [27] . All simulations were conducted with the in-house FEM software package iMOOSE.

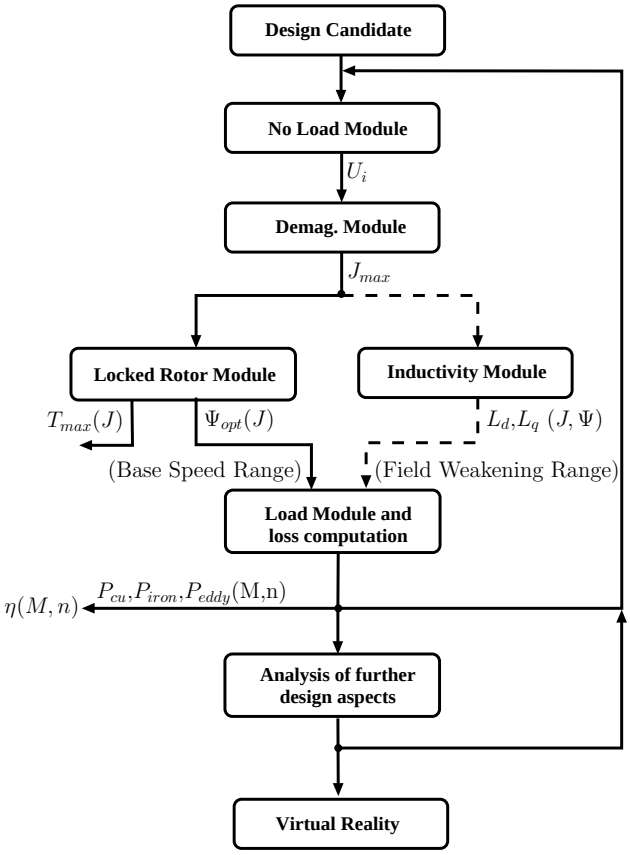

Figure 2: Flowchart of the design process for a PMSM.

Initially, a ***No-Load Simulation*** is performed to calculate the stator phase flux-linkage and the back-emf, as well as to evaluate the occurring higher harmonic field wave. Moreover, this computation step detects the position of the d- and q-axis for further processing steps.

The electromagnetic overload capability of permanent magnet (PM) motors is limited by the demagnetisation strength of the permanent magnet material. To determine the specific overload capability of a given design candidate, a ***Demagnetisation Test*** is conducted. Hence the maximum current I_{max} is determined, still having a working point on the linear part of the demagnetisation characteristic to avoid an irreversible demagnetisation.

The torque of a PMSM with internal magnets (IPMSM) ($X_q > X_d$) consists of the synchronous torque T_{syn} and the reluctance torque T_{rel} and is given by:

$$T = \underbrace{\frac{3p}{\omega} \cdot U_p I_q}_{T_{syn}} - \underbrace{\frac{3p}{\omega} \cdot I_q I_d \cdot (X_q - X_d)}_{T_{rel}} . \tag{1}$$

where p is the pole pair number, ω the angular frequency and U_p the back-emf. Inserting $I_q = I\cos\psi$, $I_d = I\sin\psi$, where ψ is the field-weakening angle, the torque can be rewritten as

$$T = \hat{T}_{syn}\cos(\psi) - \hat{T}_{rel}\sin(2\psi) \tag{2}$$

i.e. the sum of a fundamental ($\hat{T}_{syn}$) and the first harmonic ($\hat{T}_{rel}$) which are constant for a given current. For operation points in the base speed range the phase voltage U_s is below the maximum voltage, so that the phase current is constrained by the magnet demagnetization and further thermal limitations or the power electronic's maximal current. Differentiating (2) with respect to ψ, one sees that the maximum torque T_{max} per current (MTPA-control) is realised for the so called optimal field-weakening angle ψ_{opt}. The ***Locked-Rotor Test*** is thus made to determine the

absolute values of the synchronous torque $\hat{T}_{syn}$ and the reluctance torque $\hat{T}_{rel}$, as well as to determine the optimal field-weakening angle ψ_{opt} and the maximum torque T_{max}. This calculation is performed for a stepwise increasing stator-current density in order to capture the dependency of those quantities on the load current.

For operation points in the field-weakening range, the control strategy of the power converter limits the phase voltage to its maximum by shifting ψ. For the simulation of this control strategy, the direct- and quadrature-axis reactances (X_d and X_q), which are both functions of the load current and the field weakening angle ψ, are calculated by means of the X_dX_q-***Computation***. By knowing the reactances X_d and X_q and a corresponding field weakening angle the electromagnetic que for each operation point is given by (1).

In order to evaluate and rate the motor's energy consumption and efficiency, all losses are required to be determined for all operation points. This computation is conducted by the ***Operation Point Simulation***. At this step, the optimal field-weakening angle ψ_{opt} is used to set the maximum torque in the base speed range, whereas ψ has to be set by means of control strategies in the field-weakening range. Ohmic losses P_{cu} are estimated considering end winding effects. Iron losses are computed by means of quasi-static numerical FE simulations and an improved post-processing formula based on the loss-separation principle considering rotational hysteresis losses as presented in section IV. Eddy-current losses in permanent magnets are calculated for each considered operation point by means of a transient 3D-FE approach, as described in [39] and [14].

By performing the loss calculation it is possible to determine the total losses P_{tot} for each operation point. Resulting from the total losses and the input power P_{in}, the efficiency η can be calculated in function of speed and torque. The results can be visualised as two-dimensional colour maps, e.g. efficiency maps as depicted in figure 3. In order to generate such a map, the base speed region is discretised by N^1_{Map} operation points, whereas the field-weakening region is sampled by N^2_{Map} points.

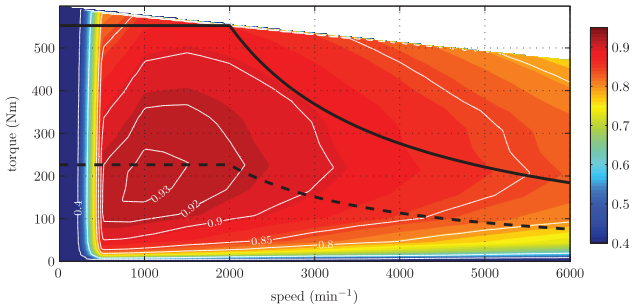

Figure 3: Exemplary result of the efficiency map of a PMSM.

B The Aspect of Parallelisation

The primary requirement of the development process for electrical machines is to simulate each design candidate over its entire torque-speed range. The proposed design process, figure 2, is capable of this by computing the non-linear machine characteristic as well as the T-n diagram by numerous 2D transient, quasi-static FE computations. As a consequence, the determination on the overall machine behaviour requires a high computational effort. This yields, in the case of a sequential processing, to a long simulation time. To limit and minimise this time delay in the design procedure, the necessary FE simulations can be processed in parallel. Reorganizing the flowchart of figure 2 into a timeline diagram shows that the response time can be shortened to a minimal duration of four FE simulations (figure 4). Since

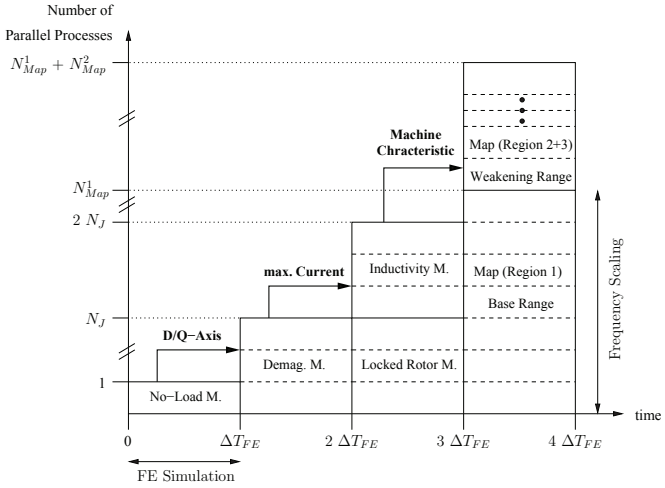

Figure 4: Parallelisation of the automated design process as timeline diagram, showing the necessary number of parallel processes in function of time.

the computational blocks, such as ***No-Load Simulation*** and ***Demagnetization Test*** are interdependent, the load is unbalanced growing with each timestep (ΔT_{Fe}), where all modules which identify the machine characteristics are carried out by a current discretisation of N_J.

The automated virtual prototyping described in section II-A and II-B has been applied in several projects. Application examples are the PMSMs developed for a parallel hybrid electric vehicle in the context of the Federal Ministry of Economics and Technology cooperative project Europa Hybrid [12], [13], [57] or for a battery electric vehicle within the framework of the Federal Ministry of Education and Research research project e-performance [1].

The next section will discuss a hybridisation of a classical conformed mapping approach for an air gap field computation of electrical machines by several FE-Reparameterations. The implementaion of such hybrid models is conducted as part of the above discussed automated tool chain for FE-Computations. By applying this, each level of hybridisation can be applied without an additional effort. By this approach, the increase of complexity and control strategy of each step does not constrain the applicability and simplicity of the model.

III Conformal Mapping and Numeric Parameterisation

Numerical methods such as the FEM are usually applied for the field calculation in electrical machines. This method is characterised by high level of detail the modelling, such as non-linear permeability of iron and exact modelling of the geometry including uncertainties due to the manufacturing. However, this approach does not allow for a detailed inside to causes-effect dependency. A well-known approach to perform the field calculation of electrical machines is based on conformal mapping (CM). This approach is based on different Ansatz-functions for different physical effects, such as slotting effects of rotor and stator field or eccentricity. In the classical approaches non-linear material properties and uncertainties can not be described. Therefore, we propose a deduction of Ansatz-functions based on of FEM simulations. The basics of the CM approach and the deduction of additional Ansatz-functions are described.

A Standard Conformal Mapping

The air gap field computation by conformal mapping is generally obtained from the solution of a linear Laplace problem, as-

suming the magnetic core has an infinite permeability. Since this system is linear, the field excitation by magnets and coils, as well the influence of the slotting, can be modelled individually.

Assuming a slotless stator, the field $\vec{B}(\Theta)$ at a certain coordinate angle Θ in the air gap, $\Theta \in [0, 2\pi[$, consists of a radial flux density $B_r(\Theta)$ and a tangential flux density $B_\varphi(\Theta)$

$$\vec{B}(\Theta) = B_r(\Theta) \cdot \vec{e}_r + B_\varphi(\Theta) \cdot \vec{e}_\varphi. \tag{3}$$

The angle dependent quantities $B_r(\Theta)$ and $B_\varphi(\Theta)$ can be expanded into a Fourier Series

$$\vec{B}(\Theta) = \sum_{n=0}^{\infty} \left(B_{r,n} \cdot \vec{e}_r + B_{\varphi,n} \cdot \vec{e}_\varphi\right) e^{\jmath np\Theta}, \tag{4}$$

where n is the frequency order and p the number of pole pairs. In this representation of the air gap field, the Fourier coefficients $B_{r,n}$ and $B_{\varphi,n}$ are the solution of a linear Laplace problem with magnets and a slotless stator depending on the magnetization configuration [63], [64], [30]. The field at a certain instance of time t due to rotor movement is given by

$$\vec{B}(t) = \vec{B} \cdot e^{\jmath\omega_r t} \tag{5}$$

where ω_r is the angular speed of the rotor.

Stator slotting significantly influences the magnetic field distribution. It is modelled by "permeance functions". These permeance functions $\vec{\lambda}$ represent the impact of slotting on the slotless field distribution and can be obtained by Schwarz-Christoffel transformations [60], [61]. Correlating the field distribution with slotting, ${}^{s}\vec{B}(t)$, with the field without slotting (5), yields the vectorial permeance $\vec{\lambda}$

$$\begin{aligned} {}^{s}\vec{B}(t) &= \vec{\lambda}^* \cdot \vec{B}(t) && (6)\\ \vec{\lambda}^* &= \begin{pmatrix} \lambda_r & \lambda_\varphi \\ -\lambda_\varphi & \lambda_r \end{pmatrix}. && (7) \end{aligned}$$

The air gap field excited by the armature current is given by

$${}^{a}\vec{B}(t, I, \psi) = \begin{pmatrix} {}^{p}\vec{B}\left(\sqrt{2}Ie^{\jmath(\omega_s t + 0^\circ)}\right) \\ {}^{p}\vec{B}\left(\sqrt{2}Ie^{\jmath(\omega_s t + 120^\circ)}\right) \\ {}^{p}\vec{B}\left(\sqrt{2}Ie^{\jmath(\omega_s t + 240^\circ)}\right) \end{pmatrix} \cdot \begin{pmatrix} e^{\jmath(\phi_q + \psi + 0^\circ)} \\ e^{\jmath(\phi_q + \psi + 120^\circ)} \\ e^{\jmath(\phi_q + \psi + 240^\circ)} \end{pmatrix}, \tag{8}$$

where ${}^{p}\vec{B}$ is the normalised field due to one phase and also obtained by conformal mapping [4]. In (8) the angle ϕ_q defines the relative phase orientation to the quadrature axis of the machine, ψ is the flux weakening angle and ω_s is the stator current angular frequency. We shall in the sequel systematically omit the coordinate Θ and the time argument t, and only indicate the dependency in I and ψ when applicable. We shall also label the quantities obtained by the conformal mapping approach with a CM exponent. The overall air gap field is thus defined as

$${}^{g}\vec{B}^{CM}(I, \psi) = {}^{a}\vec{B}^{CM}(I, \psi) + {}^{s}\vec{B}^{CM}. \tag{9}$$

B Leakage and Non-linearity

The main idea of rewriting the CM governing equations sketched in section A is to obtain a CM formulation in which each parameter represents a physically motivated quantity in order to distinguish their origin within the electromagnetic field computation. The definition of the armature field ${}^{a}\vec{B}$ in (8) includes an implicit formulation of $\vec{\lambda}$ in the Ansatz-function of the field ${}^{p}\vec{B}$. For further purposes, $\vec{\lambda}^*$ must be factorised

$${}^{g}\vec{B}^{CM}(I, \psi) = \vec{\lambda}^* \cdot \left(\vec{B}^{CM} + {}^{a}_{u}\vec{B}^{CM}(I, \psi)\right), \tag{10}$$

where an arbitrary permeance state $\vec{\lambda}$ is identical for both field fraction of ${}^{g}\vec{B}^{CM}(I, \psi)$. In (10) the auxiliary field ${}^{a}_{u}\vec{B}^{CM}(I, \psi)$ is defined by

$${}^{a}_{u}\vec{B}^{CM}(I, \psi) = \left(\vec{\lambda}^*\right)^{-1} \cdot {}^{a}\vec{B}^{CM}(I, \psi). \tag{11}$$

C Ideal Case

The comparative study [59] for modern analytical models for the electromagnetic field prediction concludes that the relative error of the air gap flux density obtained by CM with respect to FE prediction increases strongly in function of the slot-opening to slot-pitch-ratio. In order to analyse this with CM field computation, a PMSM with a slot-opening-factor of 43% is studied. The cross-section of the motor is depicted in Fig 5. All parameters

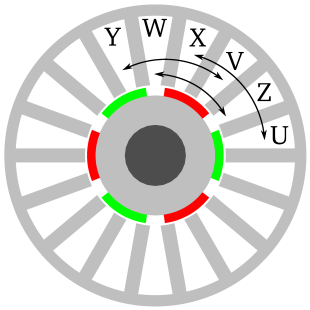

Figure 5: PMSM Cross-Section.

Table 1: PMSM Parameters.

3	Number of Pole Pairs
18	Number of Stator Teeth
0.73	Pole Pitch Factor
3 mm	Permanent Magnet Height
24.5 mm	Rotor Radius (inc. PM)
0.8 mm	Air Gap Height
54.2 mm	Outer Stator Radius
43 %	Slot Opening Factor
1.35 T	Remanence Flux Density
101 mm	Length
4 mm	Yoke Width

of the geometry and the electromagnetic evaluation are given in Table 1. The torque computation by Maxwell stress theory in case of CM is given in [23]. Figure 6(a) compares the cogging torque in function of rotor position and the corresponding time step obtained by (10) and by a FE computation where the stator is modelled as infinite permeable iron (IFEA), utilizing Neumann boundary condition. One observes that in several rotor positions the torque results are close to each other, but in other angle ranges CM overestimates the integral quantity torque, which is in agreement to the statements of [59]. The maximum deviation occurs at step three, where the edge of the magnet is aligned with the center of the slot. The corresponding flux density distribution, depicted in figure 7, shows a significant increase in its tangential component evoked by a flux path deformation in direction of the stator teeth. This effect is also known as slot leakage [46], and cannot be covered by the scalar vector quantity $\vec{\lambda}$ in (6). Adding this effect as optional correction, (10) becomes

$${}^{g}\vec{B}^{CM-Mod}(I, \psi) = \vec{\lambda}^* \cdot \left(\vec{B}^{CM} + {}^{a}_{u}\vec{B}^{CM}(I, \psi) + \Delta\vec{B}\right), \tag{12}$$

where $\Delta\vec{B}$ is the slot leakage of the rotor field. $\Delta\vec{B}$ can be determined by a single IFEA in no-load case. A comparison of the torque results in rated operation in case of IFEA and the application of (10) and (12) shows that the deviation of standard CM vanishes, see figure 6(b) and figure 7.

D Non-linear Case

The formalism in C to obtain (12) can also be applied in order to represent saturation. In this case, the permeance state $\vec{\lambda}$ turns from a constant quantity into a function of the magnitude of the current I and the flux weakening angle ψ, yielding

$${}^{g}\vec{B}^{CM}(I, \psi) = \vec{\lambda}^*(I, \psi) \cdot \left(\vec{B}^{CM} + {}^{a}_{u}\vec{B}^{CM}(I, \psi) + \Delta\vec{B}\right). \tag{13}$$

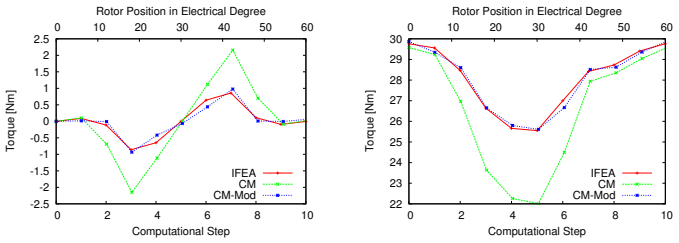

(a) Cogging Torque. (b) Torque for $J = 6\frac{A}{mm^2}$.

Figure 6: Comparison of cogging and rated torque obtained by IFEA, CM and CM-Mod.

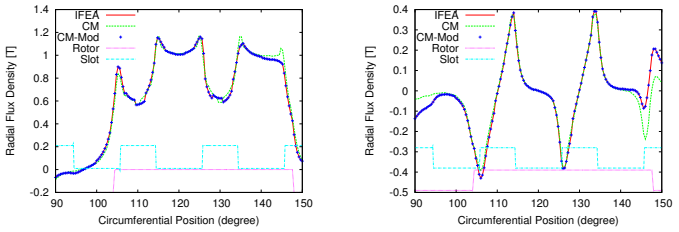

(a) B_r (b) B_φ

Figure 7: Comparison of radial and tangential flux density obtained by IFEA, CM and CM-Mod in time step three. (Rotor/Slot denote the relative geometry position).

For the evaluation of single points of interest, e.g. rated operation, $\vec{\lambda}(I,\psi)$ can be identified from a single non-linear FE simulation ${}^{g}\vec{B}^{FEA}(I,\psi)$ by

$$\vec{\lambda}(I,\psi) = \left(\vec{B}^{CM} + {}^{a}_{u}\vec{B}^{CM}(I,\psi) + \Delta\vec{B}\right)^{-*} \cdot {}^{g}\vec{B}^{FEA}(I,\psi) \tag{14}$$

to further improve the analytic field computation.

E Evaluation of cause-effect dependency

The classical CM approach lacks in the modelling of non-linear and additional parasitic effects. Still, the CM formalism, the associated time and space-harmonic analysis and the separation of different effects in Ansatz-functions deliver the possibility to separate the cause-effect dependency. Therefore, the idea is to estimate each non-ideal phenomenon by means of FEM models and deduct a corresponding Ansatz-function. Taking all Ansatz-functions into account, identical results compared to FEM are achieved. When only considering specific Ansatz-function a deeper inside to the causes of particular effects can be reached. Therefore, this method is of particular interest in the optimisation of electrical machines.

IV Calculation of Losses in Electrical Machines

The knowledge of the occurring electrical losses in an electrical machine in each operating point is eminent for an optimal design. This knowledge allows to consider the thermal conditions inside the machine for possible cooling requirements as well as the calculation of the input power and complete efficiency maps. The overall losses P_{loss} of a PM-machine are a compound of ohmic losses P_{cu} in the copper windings of the stator, the eddy current losses inside the permanent magnet volume P_{pm} as well as the iron losses P_{fe} due to varying magnetisation (in time & in space) inside the rotor and stator core:

$$P_{loss} = P_{cu} + P_{pm} + P_{fe}. \tag{15}$$

A Estimation of copper losses

The ohmic losses without skin effect for one phase can be calculated by the knowledge of the resistance of an electrical phase of the machine R_{ph} and the phase current I having stranded conductors by:

$$P_{cu,ph} = R_{ph} \cdot I^2. \tag{16}$$

B Estimation of eddy current losses in permanent magnets

According to [14], the eddy current losses in the permanent magnets P_{pm} of the electrical machine can be simulated in line with a transient 3-D FE-simulation. The simulation's output data of eddy current density J_{ec} is used by an integration over the permanent magnet's volume V_{pm}

$$P_{pm} = \int \frac{1}{\sigma_{pm}} \vec{J}_{ec}^{\,2} dV_{pm} \tag{17}$$

with the specific electrical conductivity σ_{pm} of the permanent magnet material.

C Estimation of iron losses

In the application field of efficient electrical machines there is a strong need for the accurate estimation of iron losses P_{fe} and their sources in a wide operational range of frequency f and magnetic flux density B - in particular for the electrical machines with elevated operating frequencies such as the ones incorporated into hybrid or full-electric drive trains of vehicles and the ones under power electronic supply (e.g. pulse-width modulation). Such estimation of iron losses occurring in the machine's stator and rotor parts is indispensable in order to effectively perform electromagnetic and thermal design of these electrical machines. This forms the basis for the selection of the most appropriate electrical steel grade that suits the specific working conditions in the rotating electrical machine under study. Moreover, such a development enables a deeper understanding of the specific trade-offs made during the machine design process in order to identify the particular specifications of electrical steels, which could be tailor made for specific applications. Two different approaches to estimate the iron losses are presented in the following two subsections: On the one hand, the commonly applied iron-loss is calculated in the post-processing using formula (C1.), on the other hand, an advanced approach aiming at the incorporation of the interdependence of eddy currents and hysteresis in electrical steel laminations using a magneto-dynamic hysteresis model directly in the processing step (C2.) can be applied.

C1. Post-processing iron-loss estimation

For the iron-loss modelling a 5-parameter-formula for high magnetic flux densities and high frequencies considering the non-linear material behaviour is developed by modifying the Bertotti [3] loss equation [32]. This formula utilizes the well-known loss-separation principle, that splits up the total iron losses in hysteresis losses, classical eddy current losses and excess losses, combined with an additional term for the increased eddy current loss component due to the saturated material using two additional parameters a_3 and a_4 (22). This equation is extended to be applicable to vector fields and arbitrary magnetic flux density waveforms, since in rotating electrical machines higher harmonics (in time) due to iron saturation, skin effect, stator yoke slots and the use of a power electronics supply (inverter, PWM) can occur, as well as vector magnetic fields (in space), the latter giving rise to so-called rotational losses. A Fourier-Analysis of the magnetic flux density during one electrical period serves

for the identification of the harmonic content. As a consequence the eddy current and excess loss description are extended with a summation over all harmonics [15] (20, 21). The locus of the magnetic flux density vector over one electrical period is characterized by the minimum B_{min} and maximum magnetic flux density magnitude B_{max} during this. This enables to identify the level of flux distortion. The hysteresis and excess loss terms are enhanced to model the influence of rotational and flux distortion effects (19, 21). This results in the *IEM-Formula*

$$P_{IEM} = P_{hyst} + P_{eddy} + P_{excess} + P_{sat} \tag{18}$$

with

$$P_{hyst} = a_1 \left(1 + \frac{B_{min}}{B_{max}} \cdot (r_{hyst} - 1)\right) \cdot B_{max}^2 \cdot f \tag{19}$$

$$P_{eddy} = a_2 \sum_{n=1}^{\infty} \left(B_n^2 \cdot (nf)^2\right) \tag{20}$$

$$P_{excess} = a_5 \left(1 + \frac{B_{min}}{B_{max}} \cdot (r_{excess} - 1)\right) \cdot \sum_{n=1}^{\infty} \left(B_n^{1.5} \cdot (nf)^{1.5}\right) \tag{21}$$

$$P_{sat} = a_2 a_3 B_{max}^{a_4+2} \cdot f^2 \tag{22}$$

and the magnetising frequency $f\,(\mathrm{Hz})$, the maximum value of the magnetic flux density $B_{max}\,(\mathrm{T})$, the material specific parameters $a_1 - a_5$, the rotational loss factors r_{hyst}, r_{excess}, the order of the harmonic n and the amplitude of the n-th harmonic component of the magnetic flux density $B_n\,(\mathrm{T})$. The material specific parameters $a_1 - a_5$ used in (19, 22) are identified either by a pure mathematical fitting procedure performed on measured data sets or by a semi-physical identification procedure. Figure 8 shows exemplarily the separated loss components calculated in the post-processing (19) - (22), which are used for the electromagnetic design process of an induction machine with a stator current frequency of $f = 400\,\mathrm{Hz}$ and a mechanical rotor speed of $n = 5925\,\mathrm{min}^{-1}$ and 4 pole pairs. The main contribution to each fraction of total specific losses occurs in the magnetically high exploited stator teeth. The areas of rotating magnetic fluxes can be identified by the ratio $\frac{B_{min}}{B_{max}}$ in the regions of the stator teeth back, that leads to increased specific losses in this area for (19) and (21), see figure 8(a), 8(c).

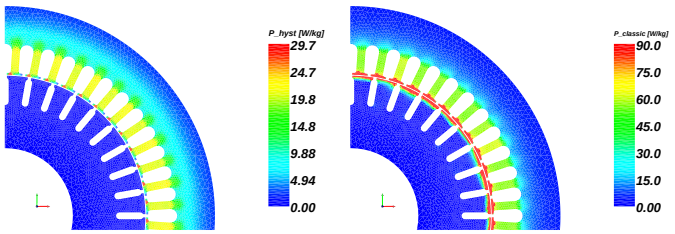

(a) Hysteresis losses

(b) Eddy current losses

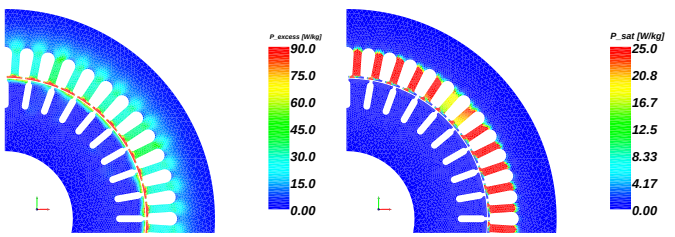

(c) Excess losses

(d) Saturation losses

Figure 8: Visualisation of the separated loss contributions of (18).

C2. Coupled magneto-dynamic hysteresis modelling

As discussed earlier, the iron losses in electrical machines are commonly estimated using empirical iron-loss models during the post-processing due to their computational advances and their satisfactory accuracy. Nevertheless, these approaches apply simplifications such as the assumption of homogeneous magnetic field distribution across the lamination and no influence of the skin effect. Additionally no minor hysteresis loops and dc-biased hysteresis effects are considered. In numerical models e.g., a non-conductive and non-dissipative soft magnetic material is assumed. The material is described by a reversible magnetisation curve. This assumption yields the entire negligence of the iron losses in the field model. However, an important aspect for the calculation of iron losses in soft magnetic materials is the consideration of the influence of non-local eddy currents, non-linear material behaviour on the field distribution and losses in electrical steel laminations as well as the interdependence between the dynamic magnetic hysteresis and the non-local eddy currents. The latter are directly induced by the externally applied time-varying magnetic field $H(t)$ in the conductive material (i.e. electrical steel sheet). These non-local eddy currents are of macroscopic nature and determined by the sample geometry. Due to the Joule effect this results in a further portion of the iron losses and the total losses resulting from the sum of both contributions (dynamic magnetic hysteresis + non-local eddy currents). The problem of modelling these non-local eddy currents is directly linked with the laminated structure of soft magnetic cores. This is the reason why the eddy current distribution in the individual laminations cannot be explicitly simulated in the FE-simulation. The measurable quantities H_{meas} and B_{meas} represent only the intrinsic material behaviour when the field is distributed homogeneously over the lamination, i.e. at low frequencies where the skin depth is larger than the sheet thickness. To overcome the aforementioned shortcomings we are developing a coupled magneto-dynamic vector-hysteresis model, which enables the modelling of dynamic vector-hysteresis loops with consideration of non-local eddy currents and the laminated structure of electrical steel grades. Therefore, an energy-based vector-hysteresis model is coupled to an one-dimensional model of half the sheet thickness of the lamination, to study the relationship between the externally applied magnetic field on the surface $H_{surface}(t)$ and the internal magnetic field $H_{material}(t)$ more accurately and to consider the influence of macroscopic eddy currents on the field distribution. In the following, both models will be briefly introduced. The used dynamic hysteresis model is based on the first law of thermodynamics, resulting in an energy-based modelling of magnetic materials [31], [33], [53] in order to characterise the non-linear behaviour of magnetic materials as well as the associated energy losses for any instant of time. This enables to go beyond the limitations of currently used models. The first law of thermodynamics (23) states that every system has an internal energy that can only be changed by the transport of work and/or heat beyond the boundaries of the system.

$$\dot{\rho}^{\Psi} = \dot{\rho}^{W} + \dot{\rho}^{Q} \tag{23}$$

A change in internal energy density $\dot{\rho}^{\Psi}$ corresponds to the work done on the system $\dot{\rho}^{W}$ plus the emitted or absorbed heat $\dot{\rho}^{Q}$. The internal energy corresponds to a reversible magnetic field strength $\vec{h}_r$ and the dissipated work within the system to an irreversible magnetic field strength $\overrightarrow{h}_{irr} = \overrightarrow{h}_i + \overrightarrow{h}_j$. Therewith the energy densities are described by

$$\dot{\rho}^{\Psi} = \overrightarrow{h}_r \cdot \dot{\overrightarrow{M}} \tag{24}$$

$$\dot{\rho}^{Q} = \overrightarrow{h}_{irr} \cdot \dot{\overrightarrow{M}}. \tag{25}$$

Deriving the energy dissipation functional (25) with respect to $\dot{\vec{M}}$ enables to represent the energy balance as a function of the magnetic field strength $\vec{h} = \vec{h}_r + \vec{h}_{irr}$. At the macroscopic level the microscopic distribution of the pinning points, hindering the domain wall motion, cannot be modelled explicitly. The pinning force can be modelled as an analogon by a dry friction force κ as in the J-A model [36]. This force counteracts any change in magnetisation and the corresponding energy density is converted into heat. Considering the dynamics of the magnetisation process, the attenuation by microscopic eddy currents can be represented as a mechanical analogue by a movement with viscous friction with the friction constant λ.

$$\vec{h}_{irr} = \frac{\partial}{\partial \dot{\vec{M}}} \left(\kappa \cdot \left| \dot{\vec{M}} \right| \right) + \frac{1}{2} \frac{\partial}{\partial \dot{\vec{M}}} \left(\lambda \cdot \dot{\vec{M}}^2 \right) \tag{26}$$

Since the energy dissipation functional is not differentiable, it models the memory effect. This enables to specify the macroscopic magnetisation with consideration of hysteresis

$$\vec{B}(\vec{h}) = \vec{M}(\vec{h}_r) + \mu_0 \cdot \vec{h}\,. \tag{27}$$

The magnetisation $\vec{M}(\vec{h}_r)$ is described by a parametric saturation curve, whose parameters are identified by measurements. To validate the identified parameters, the response of the hysteresis model is compared to measured material characteristics. A comparison of the measured losses as well as the magnetic hysteresis loops is conducted. The magnetic field $H_{meas}(t)$ used on the Epstein frame or single sheet tester serves as the model input. The model response $B_{mod}(H_{meas})$ obtained from (27) is compared to the measurement $B_{meas}(H_{meas})$(figure 9, 10).

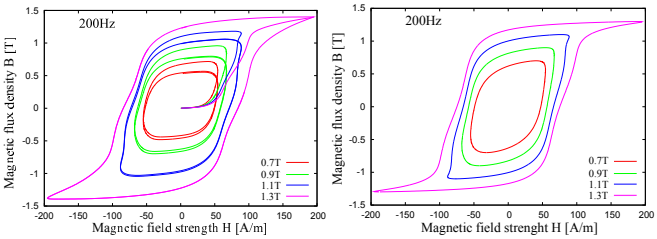

Figure 9: Comparison of modelled (left) and measured (right) hysteresis loops for M270-35A at 200Hz.

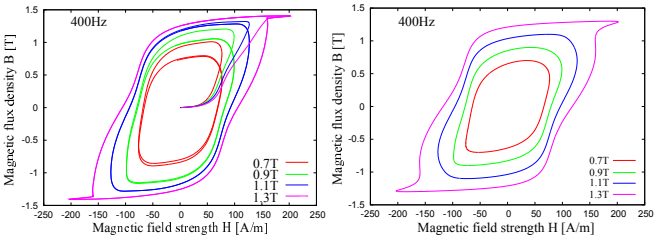

Figure 10: Comparison of modelled (left) and measured (right) hysteresis loops for M270-35A at 400Hz.

The utilisation of the 1D cross lamination model, the eddy current model of half the thickness of an individual lamination sheet can enable the nearly exact determination of the field distribution in steel laminations and improves the iron loss calculation by considering the influence of eddy currents. The relationship between the externally applied magnetic field at the surface $H_{surface}(t)$ and the internal magnetic field $H_{material}(t)$ is more precisely studied taking the influence of macroscopic eddy currents into account. In combination with the dynamic vector hysteresis model a tightly coupled transient problem is obtained that can enable nearly the exact determination of the magnetic fields and losses under the special conditions of an Epstein frame or single sheet tester. Therewith, the initial mentioned shortcoming will be reversed. With this coupled vector-hysteresis model the estimation of iron losses in a 3-dimensional FE-problem can be done in an accurate and reliable way. The input data of the vector-hysteresis model has to be the applied magnetic field H, but FE-problems for electrical machines are commonly solved by a magnetic vector potential ($\vec{A}$) approach. The resulting data for each time step is the magnetic flux density B. At the moment, the magnetic field is calculated by $H = \frac{B}{\mu_0 \mu_r}$ with the in the FE-simulation selected material data of the reluctivity $\nu(B^2)$ of the relative permeability $\mu_r = \frac{1}{\nu}$. For the future we plan to implement a magnetic scalar potential solver to provide the vector-hysteresis model directly with the resulting data (H).

V 3D ELECTRICAL MACHINE FE MODELLING WITH MOTION

Static, transient and especially field coupling simulations of electrical machines as described in section IX require the flexible displacement of the rotor by an arbitrary angle in rotating or a distance in translational electric machines. Recent studies [40] on the applicability of biorthogonal shape functions in the Finite Element analysis (FEA) of electrical machines have shown considerable potential towards a generic approach for 2D and 3D problems with motion. A standard formulation for motion problems is the moving band (MB) technique [9], which, for practical reasons, is only applicable to 2D rotating machines.

The presented non–conforming approach belongs to the category of Lagrange multiplier (LM) methods, but instead of using standard basis functions for the Lagrange multiplier, the special biorthogonal basis functions proposed in [58] are used. The biorthogonality property makes it possible to eliminate algebraically the Lagrange multiplier, turning the saddle point problem (which is typical of LM approaches) into a symmetric, positive definite system of equations. However, biorthogonal edge–based Whitney functions could not be constructed in a canonical way. In 3D, the technique can thus be applied to magnetic scalar potential $\mathbf{T}$-ω formulations, but not to magnetic vector potential $\mathbf{A}$ formulations. The implementation of the $\mathbf{T}$-ω formulation will additionally allow the estimation of iron losses by the vector-hysteresis model as described in section C2..

A Variational Formulation

Let Ω^m and Ω^s be two complementary domains called master and slave, $\Omega^m \cup \Omega^s = \Omega$, e.g. the stator and rotor of an electric machine. Let $\Gamma^m \subset \partial\Omega^m$ and $\Gamma^s \subset \partial\Omega^s$ be their common interface and $p : \Gamma^s \to \Gamma^m$ be a smooth mapping, which may account for a relative sliding between the master and the slave domain. In a magnetic scalar potential $\mathbf{T}$-ω formulation [7], the magnetic field $\mathbf{H}^k = \mathbf{T}^k - \operatorname{grad}\omega^k$, $k \in \{m, s\}$, is expressed in terms of an electric vector potential $\mathbf{T}^k$ such that $\mathbf{J}^k = \operatorname{curl}\mathbf{T}^k$ and a single–valued scalar magnetic potential ω^k. The variational calculus applied to the energy balance of the system leads to the weak formulation

$$\begin{aligned} &\sum_{k=m,s} \int_{\Omega^k} \mathbf{B}^k \cdot \operatorname{grad}\delta\omega^k \,\mathrm{d}\Omega \\ &\quad + \int_{\Gamma^s} \delta\lambda \left(\omega^s - \omega^m \circ p\right) \mathrm{d}\Gamma \\ &\quad + \int_{\Gamma^s} \lambda \left(\delta\omega^s - \delta\omega^m \circ p\right) \mathrm{d}\Gamma = 0, \end{aligned} \tag{28}$$

which must be verified for all $\delta\omega^k$ and $\delta\lambda$ fulfilling the homogeneous boundary conditions where the unknown field λ is the Lagrange multiplier.

B Discrete Formulation

In order to establish the FE equations in matrix form, the vectors of unknowns $\mathbf{u}^k$, $k \in \{m, s\}$ are divided into two blocks each. The block $\mathbf{u}_\Gamma^k$ contains the unknowns lying on the sliding interfaces Γ^k, whereas the block $\mathbf{u}_i^k$ contains the unknowns lying in the interior of the domains Ω^k. The magnetic scalar potential ω and λ are both approximated with nodal shape functions:

$$\omega^k = \sum_l \alpha_l \omega_l^k, \qquad \delta\omega^k = \{\alpha_l^k\}, \tag{29}$$

$$\lambda = \sum_l \mu_l \lambda_l, \qquad \delta\lambda = \{\mu_l\}. \tag{30}$$

The superscript ^{s} is omitted for μ because the shape functions of λ are defined on Γ^s only. From the weak formulation (28) one obtains the saddle-point problem

$$\begin{pmatrix} \mathbf{S}_{i,i}^m & \mathbf{S}_{i,\Gamma}^m & 0 & 0 & 0 \\ \mathbf{S}_{\Gamma,i}^m & \mathbf{S}_{\Gamma,\Gamma}^m & 0 & 0 & -\mathbf{M}^T \\ 0 & 0 & \mathbf{S}_{\Gamma,\Gamma}^s & \mathbf{S}_{\Gamma,i}^s & \mathbf{D}^T \\ 0 & 0 & \mathbf{S}_{i,\Gamma}^s & \mathbf{S}_{i,i}^s & 0 \\ 0 & -\mathbf{M} & \mathbf{D} & 0 & 0 \end{pmatrix} \begin{pmatrix} \mathbf{u}_i^m \\ \mathbf{u}_\Gamma^m \\ \mathbf{u}_\Gamma^s \\ \mathbf{u}_i^s \\ \boldsymbol{\lambda} \end{pmatrix} = \begin{pmatrix} \mathbf{b}^m \\ 0 \\ 0 \\ \mathbf{b}^s \\ 0 \end{pmatrix} \tag{31}$$

with

$$S_{ln}^k = \int_{\Omega^k} \bar{\mu}\, \mathrm{grad}\, \alpha_l^k \cdot \mathrm{grad}\, \alpha_n^k \, \mathrm{d}\Omega, \tag{32}$$

$$b_l^k = \int_{\Omega^k} \mathbf{T}^k \cdot \mathrm{grad}\, \alpha_l^k \, \mathrm{d}\Omega, \tag{33}$$

$$D_{jl} = \int_{\Gamma^s} \mu_j \alpha_l^s \, \mathrm{d}\Gamma, \quad M_{jl} = \int_{\Gamma^s} \mu_j \alpha_l^m \circ p \, \mathrm{d}\Gamma. \tag{34}$$

In order to obtain a symmetric positive definite system, the degrees of freedom $\mathbf{u}_\Gamma^s$ associated to the slave side Γ^s of the sliding interface and the Lagrange multiplier λ are eliminated [41]:

$$\mathbf{u}_\Gamma^s = \mathbf{D}^{-1}\mathbf{M}\mathbf{u}_\Gamma^m \equiv \mathbf{Q}\mathbf{u}_\Gamma^m, \tag{35}$$

$$\mathbf{Q} \equiv \mathbf{D}^{-1}\mathbf{M} \equiv \left(\mathbf{M}^T\mathbf{D}^{-T}\right)^T \tag{36}$$

$$\begin{pmatrix} \mathbf{S}_{i,i}^m & \mathbf{S}_{i,\Gamma}^m & 0 \\ \mathbf{S}_{\Gamma,i}^m & \mathbf{S}_{\Gamma,\Gamma}^m + \mathbf{Q}^T\mathbf{S}_{\Gamma,\Gamma}^s\mathbf{Q} & \mathbf{Q}^T\mathbf{S}_{\Gamma,i}^s \\ 0 & \mathbf{S}_{i,\Gamma}^s\mathbf{Q} & \mathbf{S}_{i,i}^s \end{pmatrix} \begin{pmatrix} \mathbf{u}_i^m \\ \mathbf{u}_\Gamma^m \\ \mathbf{u}_i^s \end{pmatrix} = \begin{pmatrix} \mathbf{b}^m \\ 0 \\ \mathbf{b}^s \end{pmatrix} \tag{37}$$

This system of equations is symmetric, positive definite and can, contrary to (31), be solved efficiently by standard Krylov subspace methods. However, to obtain (37) it is necessary to evaluate $\mathbf{D}^{-1}$, as seen in (35) and (36).

If the matrix $\mathbf{D}$ is diagonal, the evaluation reduces to a simple matrix product. This is the case when the shape functions of the Lagrange multiplier verify the following biorthogonality relation [58, 16]:

$$\begin{aligned} D_{jl} &= \int_{\Gamma^s} \mu_j \alpha_l^s \, \mathrm{d}\Gamma \\ &= \delta_{jl} \int_{\Gamma^s} \alpha_l^s \, \mathrm{d}\Gamma, \text{ with } \delta_{jl} = \begin{cases} 1 & \text{if } j = l, \\ 0 & \text{if } j \neq l, \end{cases} \end{aligned} \tag{38}$$

Previous studies have indicated that it is not feasible to construct such biorthogonal basis function for the magnetic vector potential formulation in a canonical way but for magnetic scalar potential formulation [41]. Therefore, the presented approach is applied to magnetic scalar potential $\mathbf{T}$-ω formulations.

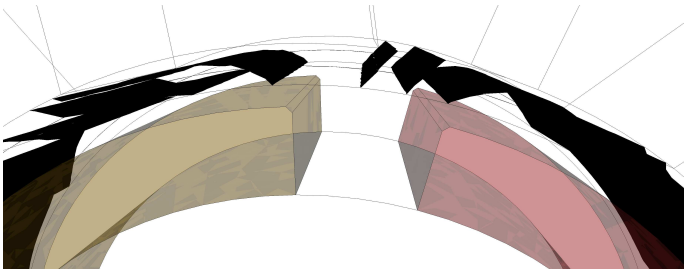

Figure 11: Isoplanes of scalar potential ω across the interface Γ in a PM-machine.

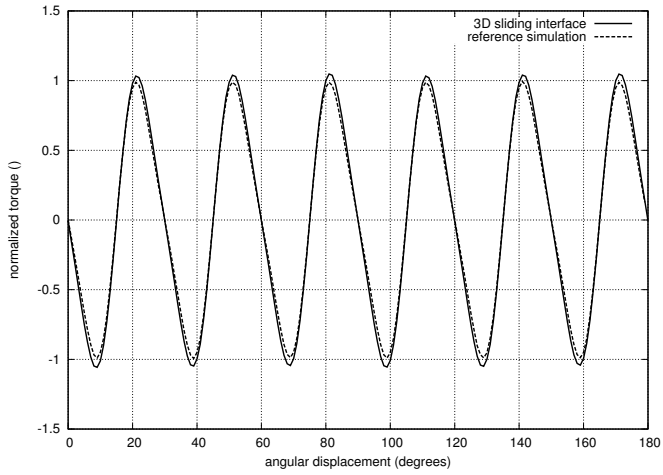

Figure 12: Comparison of resulting cogging torque with reference.

C Example application

A permanent magnet excited synchronous motor is presented as benchmark problem with scalar unknown fields. The formulations have been implemented within the institute's in-house FE-package iMOOSE [www.iem.rwth-aachen.de]. The 3D model of the motor is extruded from a 2D geometry, so that a reference solution is available. The sliding interface is a concentric cylinder in the air gap with non–conforming discretisation on the master and slave sides. The source field $\mathbf{T}^k$ of the $\mathbf{T} - \omega$ formulation is determined by the permanent magnets in this application [5]. The proposed approach would however work in the same way with a coil system. Neumann boundary conditions (no flux) apply on all external surfaces of the model. The sliding interfaces Γ^m and Γ^s intersect thus the Neumann boundary surface at the front and back ends of the model in axial direction. The restored continuity of the potential ω is controlled in figure 11 by plotting isovalue surfaces of ω and checking that they are continuos across the nonconformally discretised interface Γ. The cogging torque has been calculated and is compared with the 2D reference solution in Fig 12. It shows a very good agreement.

VI Consideration of non-ideal manufacturing

The previous studies are performed assuming ideal machines. An ideal machine presents geometrical and electric symmetric properties. Depending on the number of pole pairs p, the number of slots N and the winding configuration, the air-gap field of an ideal machine shows a spatial periodicity along its circumference. The function iterates in dependence of a certain angle. However, these characteristics will never be achieved within a real machine. The cause of this behaviour is the manufacturing process which is subjected to tolerances and therefore leads to

deviations from the ideal machine. Material dependant failures, geometrical or shape deviations may occur causing asymmetries. The assumption of an iterating air-gap field is not valid. Instead, new harmonic orders arise whereby undesired parasitic effects such as torque ripple, losses, vibrations and noise are influenced in particular.

A Causes and effects

The most studied manufacturing tolerance regarding its influence on parasitic effects in electrical machines is eccentricity [10]. Eccentriticity means that rotor and stator axis do not lie in the same location. This can be caused by bearing tolerances or deflection of the shaft. Above all, eccentricity presents a crucial influence onto the acoustical behaviour of electrical machines [55].

The properties of the applied materials are significant concerning the machine's characteristics. Due to mechanical processing of electrical steel during fabrication of electrical machines, the crystal structure of the steel is being modified [11]. This finally leads to increased iron losses.

For permanent magnet excited machines the magnet's quality is important. Not only the dimensions, but also the magnetic flux density of the magnets is subjected to tolerances. This results in varyingly strong evolved magnetic poles. This asymmetry influences the cogging torque in particular [19].

Because of their strong influence on parasitic effects, a consideration of deviations caused by manufacturing is required. It is advantageous to study this problem by use of simulations to cover a large state space. Moreover, an experimental setup is very difficult to realise because it is hardly possible to implement accurately defined faults.

As a consequence, the consideration of manufacturing tolerances in electromagnetic modelling is exemplarily presented in the following.

B Impact estimation

For the illustration of a stochastic analysis the aspect of magnet variations with magnets similar to those which are used in the given machine design is considered. The applied approach [54] is depicted in figure 13:

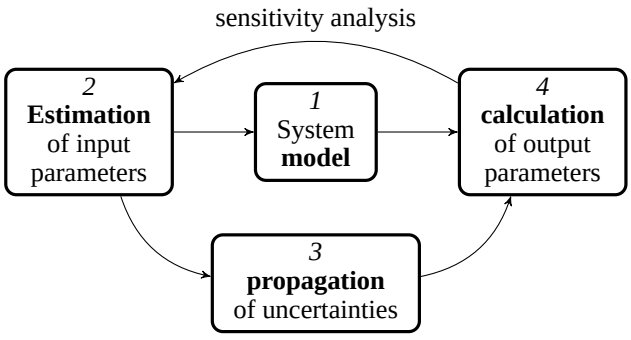

Figure 13: Chosen approach for uncertainty propagation as proposed in [54].

The beginning in stochastic considerations is the selection of a suitable model. In general all kinds of models, including analytical formulations as well as FEM models are applicable. This selection typically is influenced by the model's accuracy for the output size of interest and boundary constraints as allowed computational time. It has to be anticipated that the model's choice will strongly influence the uncertainty propagation of step 3. In this case, we decide to use a 2D-FEM model to simulate the impact of the two in figure 14 presented magnet error types onto the magnet's air field:

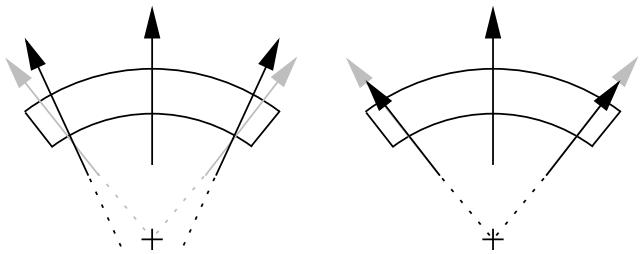

(a) Error type A: deviation of radial magnetisation towards undirectional magnetisation.

(b) Error type B: deviation of local magnetisation strength, weakening towards the magnet edge.

Figure 14: Considered variations (black) in magnet in contrast to ideal magnetisation (grey).

1. Magnetisation errors tending from radial magnetisation towards an unidirectional magnetisation as illustrated in figure 14(a). The implementation allows for an arbitrary error between both extremes, $\alpha = 0$ representing complete unidirectional magnetisation, $\alpha = 1$ representing ideal radial magnetisation.

2. Spatial changing remanence induction magnitude, shaped decreasingly from the magnet middle to the magnet border as depicted in figure 14(b), $\beta = 0$ representing a sinusoidal shaped remanence induction, $\beta = 1$ representing an ideal uniform value for the remanence induction over the entire magnet surface.

In step 2, the input distributions for both error cases were estimated. Both error cases have been chosen to be normal distributed in a way, that the maximum error of the radial component (located at a spread of 3σ) has been allowed to be 1.5%.

For the propagation of uncertainties in step 3, Monte-Carlo simulation based on a polynomial-chaos meta-model has been executed. At this point analytical models would offer the possibility of a direct uncertainty propagation, which is not possible with the FEM. Possible approaches to mitigate this problem are presented approach as well as the intrusive methods presented in [51] and [18].

Figure 15 finally shows the calculated flux-density's cumulative distribution function at the magnet's middle and enables to give error probabilities for any defined failure critera.

C Utilisation of the results

With the presented approach it is possible to evaluate the influence of manufacturing tolerances on the later produced machine. This information is valuable for the mass production of the machine and its subsequent application. Depending on the application, there are certain requirements on the machine's characteristics. Employing this methodology, it is possible to prove if – or for which percentage of the production – these characteristics can be achieved with respect to the allowed tolerance ranges.

If the requirements on the machine can not be reached, it is first of all obvious, to consider an adjustment of the allowed tolerances. However, this might be impossible or expensive to realise. The other possibility is to apply a robust design of the machine, for instance with the aim to achieve a cogging torque minimisation [35]. The general proceeding would be to define the problem at first. The parasitic effect which shall be minimised and the relevant design parameters are chosen. In a second step, it is important to employ a model which allows an accurate calculation of the interaction between the chosen design

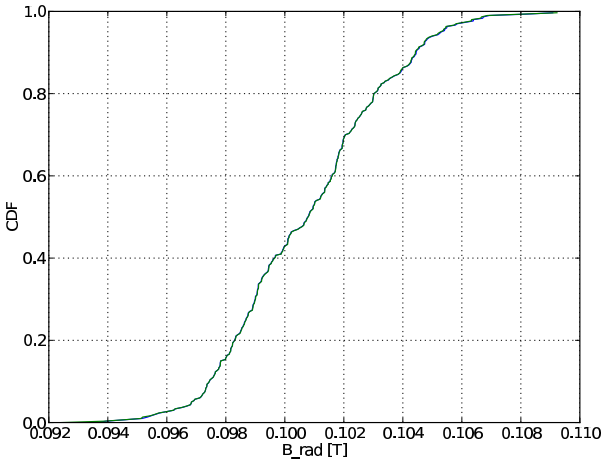

Figure 15: Cumulative distribution function (CDF) of the flux-density at the evaluation point at the magnet's middle (angle $0°$).

parameters and the target values. The third step would be to chose a convenient optimisation strategy, for instance differential evolution [8]. After performing the optimisation, the results need to be analysed and finally verified by an experimental setup.

For the described robust design, modelling is the most important factor, as the optimised machine can only be as good as the model which qualifies it. Once a good model has been developed, the resulting electromagnetic forces as well as the therefrom arising noise can be calculated, which is presented in the following section.

VII Auralisation of Electromagnetic Excited Audible Noise

For the evaluation of the radiated acoustic noise of electrical machines in variable operating conditions, a real-time auralisation procedure applicable in virtual reality environments is developed. Electromagnetic forces, structural dynamics and acoustic radiation as well as room acoustic aspects are considered. This overall task represents a multi physics problem formulation which usually consumes extreme computational efforts. The combination of electromagnetic simulation with a unit-wave response-based approach and a room acoustic virtual environment software allows for an efficient implementation. Simulation results are presented for two different types of electrical machines, an induction machine and a permanent magnet excited synchronous machine. Practical experiments are used to fine tune and validate the numerical models. A detailed description of the simulation chain can be found in [21].

A Simulationconcept

A transfer-function-based approach is applied in this work. Amplitudes of force density waves are directly linked to the free-field sound pressure on an evaluation sphere surrounding the electrical machine. In this way, a separation into off-line pre-calculation of structural and radiation data and an online-auralisation becomes possible. As shown in figure 16, the proposed concept for the auralisation of electrical machines consists of four simulation steps: The electromagnetic forces and the structural dynamic behaviour are simulated by means of the FEM. The transfer function of the mechanical structure leads to a relation between the electromagnetic force f and the surface velocity v. The sound radiation simulation yields the transfer function from surface velocity v to sound pressure p at the evaluation points in the free-field. The room acoustic transfer function

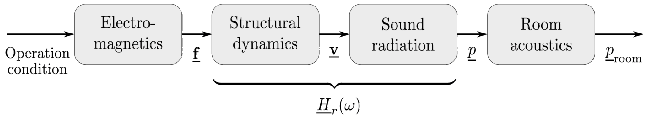

Figure 16: Schematic of transfer function-based simulation concept.

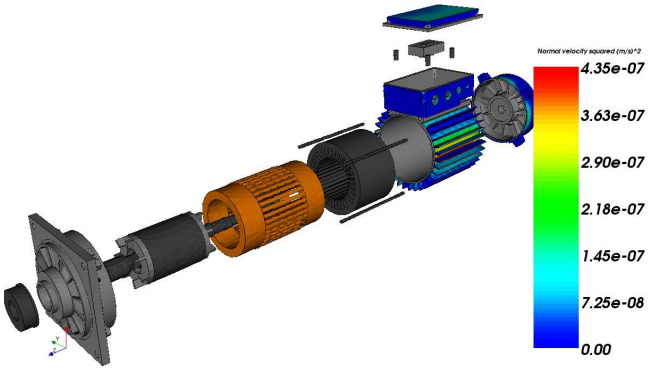

Figure 17: Structure dynamic model of an induction machine together with normal surface velocity on the housing at 533 Hz.

describes the sound propagation inside a room or car compartment from the source to a receiving position. This work only accounts for airborne sound transmission and shows the basic steps to simulate time signals for electrical drives in automotive applications. In order to include structure-borne sound transmission transfer paths have to be simulated or measured and integrated into the above-mentioned model. In the same way as the force-to-velocity transfer function is expanded in a circumferential Fourier series called force modes r, there is also one transfer function from velocity to acoustic pressure per mode. The total transfer function from force to acoustic pressure is thus denoted $H_r\,(\omega)$ for each force mode r. For each observation point and for each mode r, a transfer function from force to acoustic pressure is calculated.

B Structural dynamics

A structural dynamics simulation connects simulated electromagnetic forces and the surface velocity on the electrical machine. Commercial software packages can be used to process this simulation task by means of FEM simulations. Changes in the geometry directly require a re-run of the computationally extensive simulations. The determination of the material parameters has been found to be most critical in this step. The structural model of the electrical machine is shown in figure 17. In this case the machine is air-cooled. The results are organised in a way that the surface velocities are normalised to applied unit forces for each force mode r.

C Operational Transfer Function

As mentioned before, each block of the transfer function chain can either be studied by analytical calculation, by numerical simulation or by measurements. In this sense, there is a signal (and energy) flow from current/PM excitation, via flux density and reluctance forces, through surface velocity to sound pressure and particle velocity. For each of the three parts a transfer function can be defined, where the transfer function of the latter two typically can be considered being linear. For example, the mechan-

ical transfer function can be determined by means of numerical modal analysis (using FEM) or by means of experimental modal analysis (using shaker, accelerometer and dual-spectrum analyser), for a point excitation.

Alternatively to determining the transfer function purely from measurement, or purely from simulation and under the assumption that the operating conditions are approximately equal, we can define a mixed formulation for the transfer function as

$$H = \frac{B_{\text{meas}}}{A_{\text{simu}}}\,, \tag{39}$$

where B_{meas} is the measured output of the transfer function, and A_{simul} is the simulated input. Using magnetic forces as A_{simu} is a good choice for two reasons: First they can be simulated comparatively accurate using 2D-FEM and they are very difficult to measure. In [50], B_{meas} is chosen to be the surface acceleration and A_{simu} is indeed the magnetic force. In this case, the transfer function from the electromagnetic forces to sound pressure determined, thus the sound pressure is used as B_{meas}. The idea of formulation of the transfer function has been deduced from the well known operational modal analysis, and is therefore considered to be a valid approximation.

The starting point for the determination of transfer functions is a microphone measurement of sound pressure $p_{\text{meas}}(t)$ and a synchronised speed measurement $n(t)$ during an unloaded run-up of the PMSM with sufficiently slow slew rate. This is mapped to a so called spectrogram given by $p_{\text{meas}}(\omega, 2\pi n)$, which shows dominant lines due to harmonic force excitations, see Fig. 20. Using a peak-picking technique along these lines, allows for the definition of lines of constant order k as $p_{\text{meas}}(\omega, k),\ k = \frac{\omega}{2\pi n}$.

As a second step, it is essential to trace back each order line to a specific harmonic. This can either be done using standard table works [37], or more sophisticated even tracing back to individual field harmonics [22], the latter detailed approach is not necessary for the method proposed in this paper, it however may reveal more insight and may help trouble shooting the computer routines. For the unloaded run-up, the space vector diagrams are flat, i.e. there is no imaginary component of the force waves, due to the absence of stator currents. The Fourier decomposition of the reluctance-force-density waves reads

$$\sigma(x,t) = \sum_{k=1}^{K} \sum_{r=-R}^{R} \hat{\sigma}_{rk} \cos(rx + k \cdot 2\pi n \cdot t + \varphi)\,. \tag{40}$$

Now the assumption is made, that one harmonic force wave given by frequency harmonic number k' and by wave number r is dominant and solely accounted for at one line of constant order. Then, the FEM-to-measurement transfer function is defined as

$$H_r(\omega) = \left.\frac{p_{\text{meas}}(\omega, k)}{\hat{\sigma}_{rk}}\right|_{k=k'}\,, \tag{41}$$

where $\hat{\sigma}_{rk}$ is determined from a FEM simulation of the very geometry as the prototype delivering sound pressure measurements $p_{\text{meas}}(\omega, k)$.

The sound pressure level (SPL) for a given force excitation $\tilde{\sigma}_{rk}$ can be calculated by means of superposition:

$$L_p(\omega, n) = 20 \log_{10} \left(\sum_{k=\frac{\omega}{2\pi n}}^{K} \sum_{r=-R}^{R} \frac{\tilde{\sigma}_{rk} \cdot H_r(\omega)}{p_{\text{ref}}} \right) - \Delta_A(\omega)\,, \tag{42}$$

where $p_{\text{ref}} = 20\mu$Pa, however all results presented in this paper are referred to a slightly different undisclosed reference pressure leading to an undisclosed offset in all level plots.

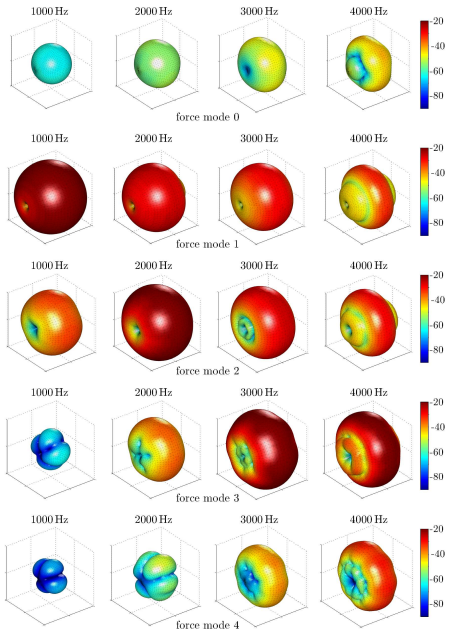

Figure 18: Sound-pressure level distribution per unit-force (dB re 20 μ Pa/Pa) for the force modes $r = 0 \ldots 4$ [21].

To compensate for the frequency dependency of the human ear, measured or simulated audible signals are passed through a filter, of which the A filter is the most common one. Therefore, (42) gives the unweighted pressure level in dB, if $\Delta_A\ (\omega) = 0, \forall\omega$ and it gives SPL in dB(A), if the A filter values are used for $\Delta_A(\omega)$.

The quadratic pressure levels of incoherent signals may be summed up immediately. Therefore, the (A-weighted) total SPL is then given by

$$L_{p,\text{tot}}(n) = 10 \log_{10} \sum_{l=1}^{N} 10^{L_p(l\omega_0, n)/10} \tag{43}$$

in dB(A), where ω_0 corresponds to the window, which was initially used to determine $p_{\text{meas}}(\omega, 2\pi n)$.

D Sound Radiation and Auralisation

The free-field sound radiation of the electrical machine can be calculated by means of the Boundary Element Method. This method requires very long computation times if higher frequencies are considered [45]. Due to the geometry of electrical machines an analytic approach exploiting cylindrical harmonics can significantly reduce the computational costs as published by the authors [20]. However, we use a different approach using measurements and only electromagnetic simulations - structural dynamics and sound radiation are not simulated explicitly as described in the section about the operational transfer function.

A PM synchronous machine is used as an example: The stator consists of a laminated sheet stack (M250-AP) with slots and a rotor made from the same material, which is equipped with surface-mounted permanent magnets ($\mu_r \sim 1$, $B_{rem} = 1.17$T). The number of stator slots is $N_1 = 6$ and the number of magnets is $2p = 4$. The transfer functions relating force densities

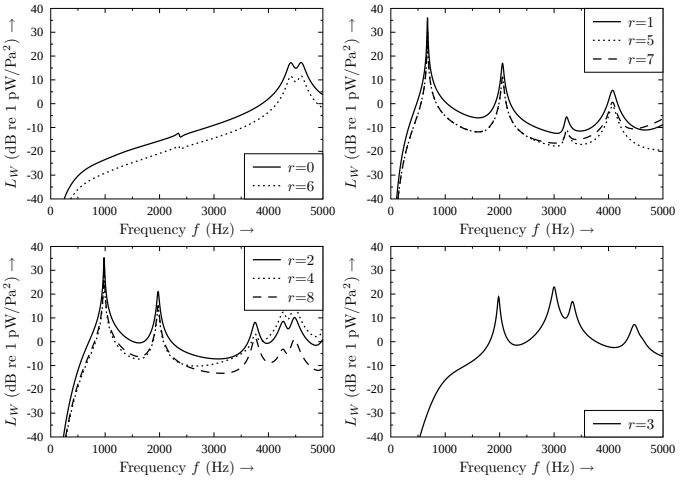

Figure 19: Sound-power level per unit-force [21].

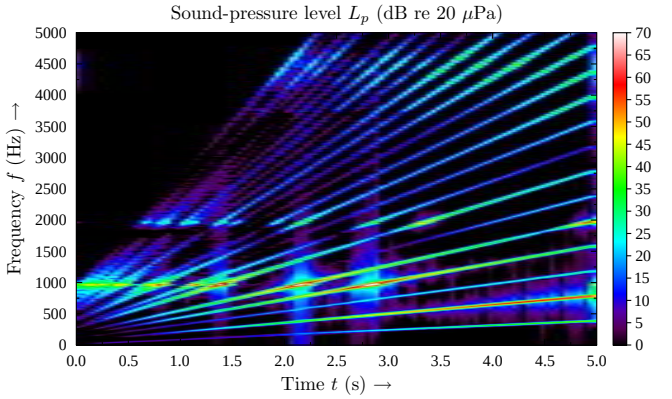

Figure 20: Spectrogram of a simulated run-up from 600 to 6000min^{-1} [21].

to sound pressure are calculated. The resulting sound pressure distributions per unit-force are shown in figure 18. It can be seen that even force orders cause a rotating velocity distribution where the radiation pattern of force order 3 indicates standing velocity distributions almost independent on frequency. Figure 19 shows the results of the unit-wave response-based approach: the sound power radiated by each force mode r. In order to simulate a run-up, sweep signals are generated up to an order of 100. Thereby, the length of the signal is set to 5 s, start and end speeds are chosen to be 600 and 6000min^{-1}. After the multiplication with the actual electromagnetic force density amplitudes, the resulting free-field sound pressure signal is obtained in 5 m distance. It is presented in form of a spectrogram shown in figure 20.

In the vicinity of certain eigen-frequencies of structural modes that are likely to be excited, the sound pressure increases significantly. In particular, those natural frequencies are located around 1, 2 and 4.5 kHz.

In figure 20, several order lines are visible. Each line is excited by a certain time-harmonic order, which is determined by the slope in the spectrogram, and by multiples of space orders. Despite this superposition of different space orders, one time harmonic order line is most commonly dominated by a single force space order.

VIII Virtual Reality

Efficient methods for the visualisation of finite element solutions are essential for the evaluation of electromagnetic devices under research and development. Important decisions are made on basis of solution visualisations and further design steps are planned on basis of the ongoing understanding of the device under research. Therefore, effective post-processing algorithms being able of handling large amounts of finite element data and the usability of such methods in an interactive way allow a faster design process.

The advantages of a graphical visualisation of the finite element solution include the ability to intuitively evaluate the numerical data regardless of data size and complexity. Furthermore, an integrated environment allows various interactive post-processing methods to obtain graphical representations, e.g. flux lines, as well as to compute integral quantities such as torque or flux.

Since many years we develope the software tool iMOOSE.trinity for visualisation of finite element field solutions, which has undergone multiple development cycles over the years and has been extended by various post-processing methods. The current version applies the Open-Source Visualization Toolkit (VTK) for the graphical representation and is designed to add pre-processing and processing facilities as long term research goals. Beside the pure visualisation of scalar and vector fields iMOOSE.trinity contains amongst others the following features and interactive post-processing capabilities:

- Flux line computation in 3D [25]
- Interactive plane cutting [24]
- Navigation through n-dimensional parameter spaces [26]
- Coupling to virtual reality (VR) systems [6]
- Support for various input devices like 3D mouse with six degrees-of-freedom

Two of these interesting features, namely computation of flux lines and coupling to professional VR systems are described in the following sections.

A Flux line computation in 3D

The design process of electrical machines benefits from the visualisation of flux lines during the post-processing of finite element data. The example chosen here is an interior permanent magnet synchronous machine (IPMSM) with rotor staggering, since in this rotor configuration stray fluxes with axial flux component are expected which are hard to locate in the solution data, and almost impractical to adequately being visualised by standard methods in 3D.

For the visualisation given in figure 21(a) an interactively placeable point widget is used as seed point for the flux line computation. By this, the user has the possibility to explore the regions of interest and locate the corresponding coordinates quickly. The placement of the seed points in the 3D machine model is done intuitively by using a 3D mouse, which offers six degrees-of-freedom. In this example, a chosen starting point in the vincinity of the permanent magnet edge, shows a stray flux line which closes through the other magnet angular to the *z*-axis. The same mechanism can be used to start a number of streams from a placed line, as exemplified in figure 21(b) for the same machine configuration without rotor skewing.

B Coupling to virtual reality systems

To improve the interactive possibilities of iMOOSE.trinity a bidirectional coupling to the VR software framework ViSTA [49] has been developed [6]. ViSTA has a scalable interface that allows its deployment in desktop workstations, small and large VR systems. The purpose of this coupling is to offer the possibility to link a simulation package with the whole range of

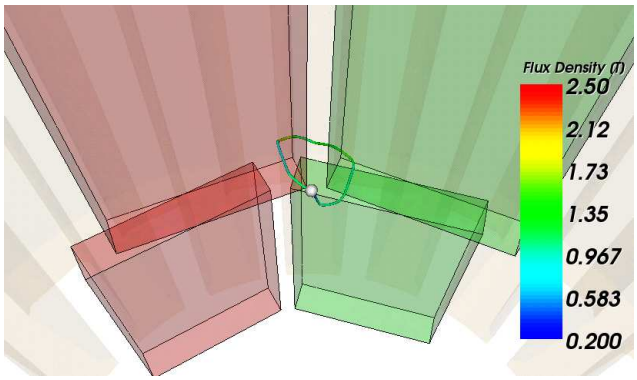

(a) Stray flux stream line between the skewed permanent magnets.

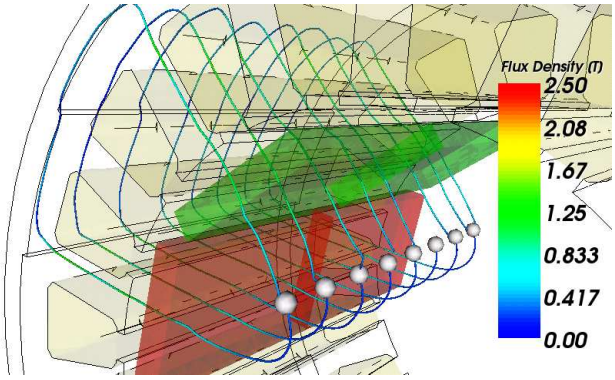

(b) Seeding points along a line below a unskewed rotors pole.

Figure 21: Interactive streamline computation and visualisation exemplified on a flux density distribution of an IPMSM with and without rotor skewing [25].

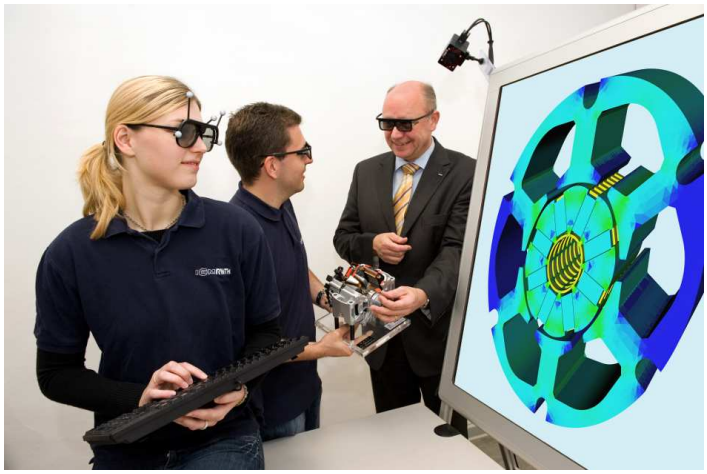

(a) Holodeck.

(b) Instrumented gloves.

Figure 22: VR devices.

immersive visualisation systems, from 3D office systems up to cave-like systems (figure 22(a)).

The underlying idea, which is in the focus of this work, is to implement such a linkage between software packages by a generalised network-based bidirectional coupling. Since techniques such as making interactive cuts or seeding particles for flow (or flux line) representation are common in both systems such a mechanism mirrors all performed actions from one system to the other, so that one ends up with a consistent representation on both environments.

The benefit in such an additional effort is to provide an extended electromagnetic processing and post-processing framework, where users employ the advantages of immersive VR-Systems, e.g. the interactive point or surface selection in 3D, by switching from the standard GUI-based finite-element environment directly to such professional VR environments. For instance, in the case of leakage flux visualisation described in the previous section, the interaction for navigating to the points of interest takes place in the VISTA driven application feeding the iMOOSE.trinity algorithm, which computes the corresponding closed magnetic flux lines.

In the future the bidirectional coupling to ViSTA can be improved by integrating VR input devices into the mirroring mechanism, so that VR controllers such as a flystick or instrumented gloves (figure 22(b)) can be utilised for electromagnetic post-processing methods.

IX Field Circuit Coupling

Within the design process of electrical drive trains the system simulation represents an important step. Modern drives do not only consist of the electrical machine but also of the power electronics and the controls, it is necessary to consider all corresponding parts to achieve a proper operation in all working points. Especially for complex control strategies such as self-sensing where saturation and inverter influences have to be taken into account this becomes very important [48, 42]. With circuit simulation software it is possible to combine the converter and the controls with an analytical representation of the machine. Since the magnetic circuit of the machine is typically designed with the help of Finite Element Analysis (FEA) in order to develop high power, highly efficient, or low noise machines [62, 56, 17] it is reasonable to take the FE model into consideration, which can substitute the analytical model completely (direct coupling) on the one hand. On the other hand it is possible to extract the linear parameters of the machine for several points of operation off-line and store them in lookup tables, that are used by the model during the simulation [44, 34]. Especially for machines that operate in magnetic saturation and for those with concentrated windings that do not entirely fulfill the assumption of a sinusoidal winding distribution [56] this simulation method can improve accuracy compared to a dq-model based simulation.

This section focusses on the extraction of lumped parameters by FEA, representing an electrical machine for the use inside a system simulation environment. A full system simulation of a PMSM servo drive using the direct coupling is applied in [56].

A Lumped parameter representation of electrical machines

Rotating electrical machines, e.g. three phase PMSMs, can be represented by an inductance matrix L^{∂}_{kl} of self and mutual inductances with dimension 3×3 and a vector of motion induced voltages e_k with dimension three. The flux induced voltage of phase k is given by the time derivative of the flux linkage ψ_k (with implicit summation over l) as the difference of the terminal voltage v_k and the ohmic voltage drop Ri_k:

$$\partial_t \psi_k = v_k - R i_k = \partial_t \psi_{kl} + \partial_t \psi_{f,k} \quad . \tag{44}$$

Herein, $\psi_{f,k} = f(\alpha)$ is the remanence flux embraced by the permanent magnets being a function of the angular position of

the rotor $\alpha = f(t)$, and $\psi_{kl} = f(\alpha, i_l)$ is the flux linkage in phase k depending on the current $i_l = f(t)$ carried by phase l and the rotor position α. Applying the differential operator in (44) yields:

$$\begin{aligned}\partial_t \psi_k &= \partial_t \left(\psi_{i,k} + \psi_{f,k}\right) \\ &= \partial_t i \partial_i \psi_{i,k} + \partial_t \alpha \partial_\alpha \psi_{\alpha,k} + \partial_t \alpha \partial_\alpha \psi_{f,k} \\ &= \left(\partial_t i_l\right) L^{\partial}_{kl} + \omega \partial_\alpha \psi_k = \left(\partial_t i_l\right) L^{\partial}_{kl} + \omega e^*_k \quad .\end{aligned} \tag{45}$$

The first term of (45) expresses the induced voltage by the flux linkage described by the inductance matrix L^{∂}_{kl} and the second term the motion induced voltage with the speed normalised electromotive force (emf) e^*_k.

B Extraction of the inductance matrix from FEA

Let

$$M_{ij}(\mathbf{a})\, a_j = b_i, \tag{46}$$

with the right hand–side (implicit summation over l)

$$b_i = \int_\Omega \mathbf{j} \cdot \boldsymbol{\alpha}_i = i_l \int_\Omega \mathbf{w}_l \cdot \boldsymbol{\alpha}_i := i_l W_{il}, \tag{47}$$

be the non-linear 2D FE equations describing the PMSM with permanent magnet excitation and stator currents. Herein, $\mathbf{j}$ is the current density and $\boldsymbol{\alpha}_i$ are the shape functions of the degrees of freedom i.e. the nodes. The magnetic vector potential is given by $\mathbf{a}$ and $\mathbf{M}$ is the non-linear system matrix arising from the Galerkin scheme, see [2]. In 2D, the current shape functions become $\mathbf{w}_k = \frac{w_l}{A_l}\mathbf{e}_z$ with w_l being the turns of phase l and A_l the corresponding turn area. Following (47), W_{il} is defined as the current shape vector with respect to phase l.

Now, let i^*_l be the currents at time t, and $b^*_i = i^*_l W_{il}$ the corresponding right–hand sides. Solving (46) with $b_i \equiv b^*_i$ and a fixed rotor angular position $\Delta\alpha = 0$ gives a^*_j and a first order linearisation around this particular solution writes

$$M_{ij}(a^*_j + \Delta a_j) = M_{ij} a^*_j + J_{ij} \Delta a_j = b^*_i + \Delta b_i \tag{48}$$

with the Jacobian matrix $J_{ij} \equiv \left(\partial_{a_j} M_{in}(a^*_j)\right) a^*_n$. Since $M_{ij} a^*_j = b^*_i$, one has

$$J_{ij}(a^*_j)\ \ \Delta a_j|_{\Delta\alpha=0} = \Delta b_i. \tag{49}$$

One can now repeatedly solve (49) with the right-hand sides $\Delta b_i = \Delta i_l\, W_{il}$ obtained by perturbing one after the other m phase currents i_l and obtain m solution vectors for $\Delta a_j|_{\Delta\alpha=0}$. Since (49) is linear, the magnitude of the perturbations Δi_l is arbitrary. One can so define by inspection the inductance matrix L^{∂}_{kl} of the electrical machine seen from terminals as

$$\begin{aligned}\Delta\psi_k|_{\Delta\alpha=0} &= W_{kj}\ \ \Delta a_j|_{\Delta\alpha=0} \\ &= W_{kj} J^{-1}_{ji}(a^*_j) W_{il}\, \Delta i_l, \equiv L^{\partial}_{kl}\, \Delta i_l\end{aligned} \tag{50}$$

with

$$L^{\partial}_{kl} = W_{kj} J^{-1}_{ji}(a^*_j) W_{il}. \tag{51}$$

Beside the extraction of the tangent inductances L^{∂}_{kl} it is also possible to extract the secant inductances L_{kl}.

C Extraction of the motion induced voltage

One can now complement (45) to account for the emf:

$$\Delta\psi_k = L^{\partial}_{kl} \Delta i_l + \omega e^*_k \tag{52}$$

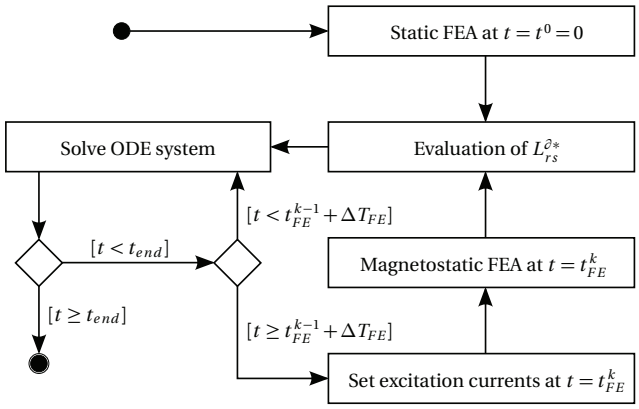

Figure 23: Transient coupling scheme FE-model and power electric circuit.

with $e^*_k \equiv \partial_\alpha \psi_k$. The direct computation of the α derivative requires to slightly shift the rotor, remesh, solve the FE problem, evaluate new fluxes and calculate a finite difference. In order to avoid this tedious process, one can again call on the energy principles. One has

$$e^*_k = \partial_\alpha \psi_k = \partial_\alpha \partial_{i_k} \Psi_M = \partial_{i_k} \partial_\alpha \Psi_M = \partial_{i_k} T \tag{53}$$

where T is the torque and Ψ_M is the magnetic energy of the system. During the identification process described above, it is possible to calculate additionally the torque corresponding to the perturbed solutions $\Delta\mathbf{a}_j|_{\Delta\alpha=0}$, and to evaluate the motion induced voltage e_k of each phase k as the variation of torque with the perturbation of the corresponding phase current i_k.

However, as the torque is a non-linear function of the fields, the perturbations need in this case to be small. Because of the linearity of (49), one may scale the perturbation currents in (53) which yields:

$$e^*_k = \frac{T(\mathbf{a}^*) - T(\mathbf{a}^* + \lambda \Delta\mathbf{a}|_{\Delta\alpha=0})}{\lambda \Delta i_k} \text{ with } \lambda = \kappa \frac{||\mathbf{a}^*||_2}{||\Delta\mathbf{a}||_2}. \tag{54}$$

Herein, the scale factor is chosen between $0.01 \leq \kappa \leq 0.05$.
The current and position dependent excitation flux is extractable as well. This is useful if the modelling of the machine follows the approach described in [34].

D Coupling to a circuit simulator

The decoupled solution of the field and the circuit problems require a time stepping scheme to coordinate the interaction of the utilised FE-solver and the circuit simulator.

The basic scheme is shown in figure 23. The time step width of the magnetostatic FE simulation is constant while the time step width of the circuit simulator is freely chosen by the simulator. The cosimulation starts with a static FE analysis to evaluate the initial lumped parameters, i.e., the tangent inductance matrix L^{∂} and the motion induced voltages e^*.

For the calculation of the motor currents two designs are feasible. The first one is the determination of the currents outside the circuit simulator generating a signal given to signal controlled current sources within the circuit simulator. Therefore, the line currents of the machine are calculated by (44) and (45) after being transformed to

$$i = (L^{\partial})^{-1} \int (v - Ri - \omega e^*) \mathrm{d}t \quad . \tag{55}$$

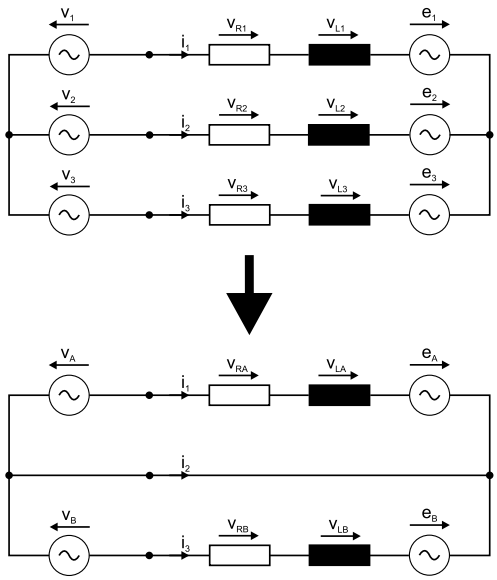

Figure 24: Reducing of circuit elements to solve overdetermination.

The terminal voltages of the machine are the voltages over these current sources. The second design is the modelling of the motor inductance, resistance, and induced voltage directly within the circuit simulator. For this purpose the simulation software has to provide controllable mutual inductances.
If the global simulation time reaches $t \geq t_{FE}^{k-1} + \Delta T_{FE}$, the phase currents of the circuit simulator are transfered to the FE-solver and step k of the magnetostatic FE-system is calculated followed by the identification of the lumped parameters L_{kl}^{∂} and e_k^*. Returning the new set of parameters to the circuit simulator the transient circuit analysis proceeds until $t \geq t_{end}$ is reached.
The variable time step width of the circuit simulator allows it to adapt the step width according to the requirements of the high frequency switching components of the circuit domain.
Since there is no zero phase-sequence system, the current equation above is overdetermined if solved independently for each phase. To solve this over-determination the system is transformed as shown in figure 24. Now, only two phase currents are calculated whereas the third is given by Kirchhoff‘s law.

E Use of the parameter extraction for control design

By the reason that the capability of a machine control is strongly dependent on its parametrisation the extraction methods that are used for the field circuit coupling described above can help to identify the required lumped parameters of the machine for the control design. Since the control design needs both, the secant and the tangent inductances, as well as the induced voltages or excitation fluxes, the extraction method delivers all required parameters for a current and position dependent control design. Especially advanced control strategies like the sensorless control profit by an accurate determination of the machine parameters [38]. For this purpose the parameters can be transformed into the d-q reference frame.

X Conclusions

Numerical computation of electrical machines still is challenging. In order to give an innovative impulse to the aspects of computation in electromagnetics, a state-of-the-art design methodology for electrical machines has been presented, starting with the presentation of an automated calculation chain. Extended conformal mapping for faster simulations as well as cause-effect analysis has been presented, leading to a detailed investigation methodology for loss computation. Since the advanced dynamic hysteresis approach requires the magnetic scalar potential, solver considerations have been presented subsequently. As all models until here assumed a symmetric machine behaviour, stochastic analysis of electrical machines has been discussed, followed by notions about the calculation of acoustics and the machine presentation in VR. The paper concludes with the calculation of lumped parameters, allowing finally to build models for the machine controls. Following this design chain enables a better understanding of the computation and analysis of electromagnetic devices such as an eletrical machine.

XI References

[1] Audi AG: *Forschungsprojekt e-performance*. http://www.audi.de/eperf/brand/de.html. version: May 2012

[2] Bastos, J. P. a. ; Sadowski, N: *Electromagnetic Modeling by Finite Element Methods*. Taylor & Francis, 2003. – ISBN 0824742699

[3] Bertotti, G: “General Properties of Power Losses in Soft Ferromagnetic Materials”. *Magnetics, IEEE Transactions on* 24 (1989), vol. 1, p. 621–630

[4] Binns, K. J.: *Analysis and computaion of electric and magnetic field problems,*. Pergamon Press, 1963

[5] Biro, O ; Preis, K ; Vrisk, G ; Richter, K. R. ; Ticar, I: “Computation of 3-D magnetostatic fields using a reduced scalar potential”. *IEEE Transactions on Magnetics* 29 (1993), March, vol. 2, p. 1329–1332. – ISSN 0018–9464

[6] Buendgens, D ; Hamacher, A ; Hafner, M ; Kuhlen, T ; Hameyer, K: “Bidirectional Coupling Between 3-D Field Simulation and Immersive Visualization Systems”. *Magnetics, IEEE Transactions on* 48 (2012), Feb, vol. 2, p. 547 –550. – ISSN 0018–9464

[7] Carpenter, C ; Wyatt, E: “Efficiency of numerical techniques for computing eddy currents in two and three dimensions”. *Proc. COMPUMAG*. Oxford, April 1976, p.242–250

[8] Das, S ; Suganthan, P: “Differential Evolution: A Survey of the State-of-the-Art”. *Evolutionary Computation, IEEE Transactions on* 15 (2011), Feb., vol. 1, p. 4 –31. – ISSN 1089–778X

[9] Davat, B ; Ren, Z ; Lajoie-Mazenc, M: “The movement in field modeling”. *Magnetics, IEEE Transactions on* 21 (1985), vol. 6, p. 2296–2298. – ISSN 0018–9464

[10] Ebrahimi, B ; Faiz, J: “Diagnosis and performance analysis of threephase permanent magnet synchronous motors with static, dynamic and mixed eccentricity”. *Electric Power Applications, IET* 4 (2010), january, vol. 1, p. 53 –66. – ISSN 1751–8660

[11] Emura, M ; Landgraf, F ; Ross, W ; Barreta, J: “The influence of cutting technique on the magnetic properties of electrical steels”. *Journal of Magnetism and Magnetic Materials* 254 (2003), jan, p. 358 –360

[12] Finken, T ; Hameyer, K: “Design and optimization of an IPMSM with fixed outer dimensions for application in HEVs”. *IEEE International Conference on Electric Machines and Drives, IEMDC*, 2009, p. 1743–1748

[13] Finken, T ; Hafner, M ; Felden, M ; Hameyer, K: “Design rules for energy efficient IPM motors in HEV applications”. *ELECTROMOTION* 17 (2010), July, vol. 3, p. 143–154. – ISSN 1223–057X

[14] Finken, T ; Hameyer, K: “Computation of Iron- and Eddy-Current Losses in IPM Motors depending on the Field-Weakening Angle and Current Waveform”. *Przeglad Elektrotchniczny* 5 (2010), May, p. 123–128. – ISSN 0033–2097

[15] Fiorillo, F ; Novikov, A: “Power losses under sinusoidal, trapezoidal and distorted induction waveform”. *Magnetics, IEEE Transactions on* 26 (1990), vol. 5, p. 2559–2561

[16] Flemisch, B ; Wohlmuth, B: “Nonconforming Discretization Techniques for Coupled Problems”. Helmig, R (Hrsg.) ; Mielke, A (Hrsg.) ; Wohlmuth, B (Hrsg.): *Multifield Problems in Solid and Fluid Mechanics* Bd. 28. Springer Berlin / Heidelberg, 2006, p. 531–560

[17] Franck, D ; Giet, M van d. ; Burdet, L ; Coleman, R ; Hameyer, K: “Simulation of Acoustic Radiation of an AC Servo Drive Verified by Measurements”. *International Symposium on electromagnetic fields, ISEF*. Arras, France, September 2009

[18] Gaignaire, R ; Clenet, S ; Moreau, O ; Sudret, B: “Current Calculation in Electrokinetics Using a Spectral Stochastic Finite Element Method”. *Magnetics, IEEE Transactions on* 44 (2008), June, vol. 6, p. 754 –757. – ISSN 0018–9464

[19] Gasparin, L ; Cernigoj, A ; Markic, S ; Fiser, R: “Additional Cogging Torque Components in Permanent-Magnet Motors Due to Manufacturing Imperfections”. *Magnetics, IEEE Transactions on* 45 (2009), march, vol. 3, p. 1210 –1213. – ISSN 0018–9464

[20] Giet, M van d. ; Müller-Trapet, M ; Dietrich, P ; Pollow, M ; Blum, J ; Hameyer, K ; Vorländer, M: “Comparison of acoustic single-value parameters for the design process of electrical machines”. *39th International Congress on Noise Control Engineering INTER-NOISE*. Lisbon, Portugal, June 2010

[21] Giet, M van d.: *Analysis of electromagnetic acoustic noise excitations:: A contribution to low-noise design and to the auralization of electrical machines*. 1., Aufl. Shaker, 2011. – ISBN 3832299734. – Dissertation, Institute of electrical Machines, RWTH-Aachen University

[22] Giet, M van d. ; Rothe, R ; Herranz Gracia, M ; Hameyer, K: “Analysis of noise exciting magnetic force waves by means of numerical simulation and a space vector definition”. *18th International Conference on Electrical Machines, ICEM 2008*. Vilamoura, Portugal, September 2008

[23] Hafner, M ; Franck, D ; Hameyer, K: “Static Electromagnetic Field Computation by Conformal Mapping in Permanent Magnet Synchronous Machines”. *Magnetics, IEEE Transactions on* 46 (2010), vol. 8, p.3105–3108. – ISSN 0018–9464

[24] Hafner, M ; Schöning, M ; Antczak, M ; Demenko, A ; Hameyer, K: “Interactive Postprocessing in 3D Electromagnetics”. *Magnetics, IEEE Transactions on* 46 (2010), vol. 8, p. 3437–3440. – ISSN 0018–9464

[25] Hafner, M ; Schöning, M ; Antczak, M ; Demenko, A ; Hameyer, K: “Methods for Computation and Visualization of Magnetic Flux Lines in 3-D”. *Magnetics, IEEE Transactions on* 46 (2010), vol. 8, p. 3349–3352. – ISSN 0018–9464

[26] Hafner, M ; Böhmer, S ; Henrotte, F ; Hameyer, K: “Interactive visualization of transient 3D electromagnetic and n-dimensional parameter spaces in virtual reality”. *COMPEL* 30 (2011), May, vol. 3, p. 906–915. – ISSN 0332–1649

[27] Hafner, M ; Finken, T ; Felden, M ; Hameyer, K: “Automated Virtual Prototyping of Permanent Magnet Synchronous Machines for HEVs”. *IEEE Transactions on Magnetics* 47 (2011), May, vol. 5, p. 1018–1021. – ISSN 0018–9464

[28] Hameyer, K ; Driesen, J ; De Gersem, H ; Belmans, R: “The classification of coupled field problems”. *Magnetics, IEEE Transactions on* 35 (1999), May, vol. 3, p. 1618 – 1621. – ISSN 0018–9464

[29] Hameyer, K ; Belmanns, R: *Numerical modelling and design of electrical machines and devices* -. WIT Press, 1999. – ISBN 978–1–853–12626–0

[30] Hanselman, D. C.: *Brushless Permanent Magnet Motor Design*. 2. The Writers’ Collective, 2003. – ISBN 1932133631

[31] Henrotte, F ; Hameyer, K: “A dynamical vector hysteresis model based on an energy approach”. *Magnetics, IEEE Transactions on* 42 (2006), p. 899–902

[32] Henrotte, F ; Hameyer, K: “Modern Methods for iron loss computation”. *International Conference on Magnetism and Metallurgy*. Freiberg, Germany, 2010

[33] Henrotte, F ; Nicolet, A ; Hameyer, K: “An energy-based vector hysteresis model for ferromagnetic materials”. *COMPEL* 25 (2006), vol. 1, p. 71–80

[34] Herold, T ; Franck, D ; Lange, E ; Hameyer, K: “Extension of a d-q model of a permanent magnet excited synchronous machine by including saturation, cross-coupling and slotting effects”. *Electric Machines Drives Conference (IEMDC), 2011 IEEE International*, 2011, p. 1363 –1367

[35] Islam, M ; Islam, R ; Sebastian, T ; Chandy, A ; Ozsoylu, S: “Cogging Torque Minimization in PM Motors Using Robust Design Approach”. *Industry Applications, IEEE Transactions on* 47 (2011), july-aug., vol. 4, p. 1661 –1669. – ISSN 0093–9994

[36] Jiles, D. C. ; Atherton, D. L.: “Theory of ferromagnetic hysteresis”. *Journal of Magnetism and Magnetic Materials* 61 (1986), p. 48–60

[37] Jordan, H: *Geräuscharme Elektromotoren*. W. Girardet, 1950

[38] Jurkovic, S ; Strangas, E: “Cross-saturation effects on position estimation using BEMF methods in PMAC machines”. *Electric Machines Drives Conference (IEMDC), 2011 IEEE International*, 2011, p. 7 –12

[39] Kaehler, C ; Henneberger, G: “Eddy-current computation in the claws of a synchronous claw-pole alternator in generator mode”. *Magnetics, IEEE Transactions on* 38 (2002), March, vol. 2, p. 1201 –1204. – ISSN 0018–9464

[40] Lange, E ; Henrotte, F ; Hameyer, K: “A Variational Formulation for Nonconforming Sliding Interfaces in Finite Element Analysis of Electric Machines”. *Magnetics, IEEE Transactions on* 46 (2010), vol. 8, p.2755–2758. – ISSN 0018–9464

[41] Lange, E ; Henrotte, F ; Hameyer, K: “Biorthogonal Shape Functions for Nonconforming Sliding Interfaces in 3-D Electrical Machine FE Models With Motion”. *Magnetics, IEEE Transactions on* 48 (2012), vol. 2, p. 855–858

[42] Li, Y ; Zhu, Z ; Howe, D ; Bingham, C: “Modeling of Cross-Coupling Magnetic Saturation in Signal-Injection-Based Sensorless Control of Permanent-Magnet Brushless AC Motors”. *Magnetics, IEEE Transactions on* 43 (2007), June, vol. 6, p. 2552 –2554. – ISSN 0018–9464

[43] Lowther, D ; Silvester, P: *Computer-aided design in magnetics* -. Berlin Heidelberg New York : Springer-Verlag, 1986. – ISBN 978–0–387–15756–6

[44] Mohammed, O ; Liu, S ; Liu, Z: “A phase variable model of brushless dc motors based on finite element analysis and its coupling with external circuits”. *Magnetics, IEEE Transactions on* 41 (2005), may, vol. 5, p. 1576 – 1579. – ISSN 0018–9464

[45] Müller-Trapet, M ; Dietrich, P ; Giet, M van d. ; Blum, J ; Vorländer, M ; Hameyer, K: “Simulated Transfer Functions for the Auralization of Electrical Machines”. *European Acoustics Association, EAA-Euroregio*. Ljubljana, Slovenia, September 2010

[46] Oberretl, K: “Die Berechnung des Streuflusses im Luftspalt von elektrischen Maschinen mit Kaefig- oder Daempferwicklung. Teil I: Theorie und Berechnungs Methoden.”. *Archiv fur Elektrotechnik Berlin* 69 (1986), vol. 1, p. 11–22. – ISSN 00039039

[47] Reece, A. B. J. ; Preston, T. W.: *Finite Element Methods in Electrical Power Engineering* -. New York : Oxford University Press, 2000. – ISBN 978–0–198–56504–8

[48] Reigosa, D ; Garcia, P ; Raca, D ; Briz, F ; Lorenz, R: “Measurement and Adaptive Decoupling of Cross-Saturation Effects and Secondary Saliencies in Sensorless Controlled IPM Synchronous Machines”. *Industry Applications, IEEE Transactions on* 44 (2008), Nov.-Dec., vol. 6, p. 1758 –1767. – ISSN 0093–9994

[49] Reimersdahl, T van ; Kuhlen, T ; Gerndt, A ; Henrichs, J ; Bischof, C: “ViSTA: a multimodal, platform-independent VR-Toolkit based on WTK, VTK, and MPI”. *Fourth International Immersive Projection Technology Workshop (IPT2000)*. Ames, Iowa, 2000

[50] Roivainen, J: *Unit-wave response-based modeling of electromechanical noise and vibration of electrical machines*, Helsinki University of Technology, Diss., 2009

[51] Rosseel, E ; De Gersem, H ; Vandewalle, S: “Spectral Stochastic Simulation of a Ferromagnetic Cylinder Rotating at High Speed”. *Magnetics, IEEE Transactions on* 47 (2011), may, vol. 5, p. 1182 –1185. – ISSN 0018–9464

[52] Silvester, P. P. ; Ferrari, R. L.: *Finite Elements for Electrical Engineers* -. 3. Aufl. Cambridge : Cambridge University Press, 1996. – ISBN 978–0–521–44953–3

[53] Steentjes, S ; Eggers, D ; Hameyer, K: “Application and verification of a dynamic vector-hysteresis model”. *Magnetics, IEEE Transactions on* (accepted for publication)

[54] Sudret, B: *Uncertainty propagation and sensitivity analysis in mechanical modesl - Contributions to structural reliability and stochastic spectral methods*, Universite BLAISE PASCAL - Clermont II, Ecole Doctorale Sciences pour l’Ingenieur, Diss., 2007

[55] Torregrossa, D ; Khoobroo, A ; Fahimi, B: “Prediction of Acoustic Noise and Torque Pulsation in PM Synchronous Machines With Static Eccentricity and Partial Demagnetization Using Field Reconstruction Method”. *Industrial Electronics, IEEE Transactions on* 59 (2012), Feb., vol. 2, p. 934 –944. – ISSN 0278–0046

[56] Tsai, M ; Weng, M ; Hsieh, M: “Computer-aided design and analysis of new fan motors”. *Magnetics, IEEE Transactions on* 38 (2002), Sep, vol. 5, p. 3467 – 3474. – ISSN 0018–9464

[57] TÜV Rheinland: *Verbundprojekt Europa-Hybrid, Innovativer PKW-Hybridantrieb für Europa*. http://www.hybrid-antriebe.org/web/index.php?id=82. version: May 2012

[58] Wohlmuth, B. I.: “A Mortar Finite Element Method Using Dual Spaces for the Lagrange Multiplier”. *SIAM Journal on Numerical Analysis* 38 (2001), vol. 3, p.989–1012. – ISSN 00361429

[59] Wu, L ; Zhu, Z ; Staton, D ; Popescu, M ; Hawkins, D: “Comparison of analytical models for predicting cogging torque in surface-mounted PM machines”. *Electrical Machines (ICEM), 2010 XIX International Conference on*, 2010, p. 1–6

[60] Zarko, D ; Ban, D ; Lipo, T: “Analytical calculation of magnetic field distribution in the slotted air gap of a surface permanent-magnet motor using complex relative air-gap permeance”. *Magnetics, IEEE Transactions on* 42 (2006), vol. 7, p. 1828–1837. – ISSN 0018–9464

[61] Zarko, D ; Ban, D ; Lipo, T: “Analytical Solution for Cogging Torque in Surface Permanent-Magnet Motors Using Conformal Mapping”. *Magnetics, IEEE Transactions on* 44 (2008), vol. 1, p. 52–65. – ISSN 0018–9464

[62] Zhao, C hui ; Qin, H ; Yan, Y guang: “Analysis of the Pole Numbers on Flux and Power Density of IPM Synchronous Machine”. *Power Electronics and Drives Systems, 2005. PEDS 2005. International Conference on* Bd. 2, 2005, p. 1402 –1407

[63] Zhu, Z ; Howe, D: “Instantaneous magnetic field distribution in brushless permanent magnet DC motors. III. Effect of stator slotting”. *Magnetics, IEEE Transactions on* 29 (1993), vol. 1, p. 143–151. – ISSN 0018–9464

[64] Zhu, Z ; Howe, D ; Chan, C: “Improved analytical model for predicting the magnetic field distribution in brushless permanent-magnet machines”. *Magnetics, IEEE Transactions on* 38 (2002), vol. 1, p. 229–238. – ISSN 0018–9464

Authors name and Affiliation

Kay Hameyer, Stefan Böhmer, Isabel Coenen, Daniel Eggers, Matthias Felden, David Franck, Martin Hafner, François Henrotte, Thomas Herold, Marco Hombitzer, Enno Lange, Peter Offermann, Björn Riemer, Simon Steentjes.

Institute of Electrical Machines,
RWTH-Aachen University,
Schinkelstrasse 4, D-52056 Aachen, Germany,
post@iem.rwth-aachen.de,

www.iem.rwth-aachen.de